Impacts of fault-sill interactions on sill emplacement in the Vøring Basin, Norwegian North Sea.

Siregar, Einstein[1]; Omosanya, Kamaldeen.O[2,3,4], Magee, Craig[5] Johansen, Ståle.E[1].

[1] Department of Geoscience and Petroleum, Norwegian University of Science and Technology, Trondheim.
[2]Stiftelsen for industriell og teknisk forskning (SINTEF) Petroleum, 7465, Trondheim
[3]Timelapsegeo AS, Stiklestadveien 1, 7041 Trondheim.
[4]The Research Centre for Arctic Petroleum Exploration, ARCEx.
[5] Institute of Geophysics and Tectonics, School of Earth and Environment, University of Leeds, Leeds, LS2 9JT, UK.

Corresponding author: kamaldeen.o.omosanya@ntnu.no

Abstract

Pre-existing faults may facilitate subsurface magma transport and sill trangression in sedimentary basins. Although widely recognized, interaction between faults and intrusion networks in sedimentary basins remains poorly imaged by seismic reflection data. To understand how sills interact with pre-existing faults in sedimentary basins, we use high-resolution 3-D seismic reflection data from the Naglfar Dome, Vøring Basin to examine the seismic expression of sills, interpret fault geometries and displacement patterns, and characterize sill-fault interactions. The sills are expressed as tuned reflection packages, meaning they are below ~<50±5 m thick, with saucer-shaped, transgressive, and strata-concordant morphologies that range in area from 6 km^2 to 180 km^2. The interconnected sills form a sill-complex, which was emplaced in the Eocene and cross-cuts three main stratigraphic intervals (i.e. Nise, Tang, and Brygge Formations). Faults are of Early Paleocene to Early Eocene age, tectonic in origin and dominated by normal faults that are up to 28 km long. Fault and sill interactions define a spectrum, which we sub-divide into five categories (i.e. Type 1a, 1b, 2, 3 and 4); the two main end-member fault-sill relationships documented here are (a) sills stepping up stratigraphy via faults and (b) those with their inclined segments intruded along fault planes. Whilst interactions between the faults and the sills are common, quantitative displacement analysis reveals fault displacement did not influence where sills exploited faults. In the study, the intricate interaction of fault and magmatic sills and its broader implications to structural compartmentalization and outcrop-scale studies in many magma-rich continental margins are demonstrated.

Keywords: Magma, sills, faults, intersection geometries, emplacement, plumbing, Vøring Basin.

1. Introduction

Sills and sill-complexes occur in a wide range of sedimentary basins worldwide (e.g. Delaney et al., 1986; Mcclay and Ellis, 1987; Skogseid et al., 1992; Planke et al., 2005; Cartwright and Hansen, 2006; Bédard et al., 2012; Schofield et al., 2012; Magee et al., 2013b; Magee et al., 2013c). Whilst many intrusion-bearing sedimentary basins contain arrays of faults, the interaction between magma plumbing systems and fault networks remains poorly understood. The utilisation of 3-D seismic reflection data, coupled with outcrop-scale studies, have shown that sills may cross-cut, step-up, or intrude along pre-existing fault planes (e.g. Valentine and Krogh, 2006; Bédard et al., 2012; Magee et al., 2013b). These studies suggest fault-sill interactions may be controlled by fault connectivity, geometry, orientation, and/or fault rock properties (Valentine and Krogh, 2006; Bédard et al., 2012; Magee et al., 2013b).

Here, we address the role of fault-sill interactions in controlling magma plumbing systems by using the Naglfar Dome, offshore Norway as a natural laboratory where several studies have documented sill emplacement (e.g. Skogseid et al., 1992; Skogly, 1998; Svensen et al., 2003; Planke et al., 2005; Omosanya et al., 2017; Omosanya et al., 2018). Sill emplacement in the Naglfar Dome, Mid-Norwegian continental margin (Figure 1) was associated with the opening of the Norwegian-Greenland Seas during the Early Cenozoic (Lundin and Doré, 2002; Omosanya et al., 2017). Sills were emplaced during various pulses of magmatism in the Early Cenozoic and periodically interacted with a complex array of normal and inverted faults (Hansen, 2004; Hansen and Cartwright, 2006a, b). Our study focuses on some fundamental questions regarding the interaction of faults and sills, including: (a) what is the timing of sill emplacement in the study area, relative to fault activity (i.e. nucleation, reactivation, and/or inversion)?; (b) what is the style of fault-sill interactions in 3-D?; and (c) does fault kinematic history influence their capability to act as conduits or barriers to magma flow?

2. Geological setting

The location of our study area is between latitude 62° and 69° N along the Mid-N orwegian continental margin within a region that consists of the Møre and the Vøring Basins (Figure 1; Brekke et al., 1999). We focus on the Vøring Basin, which is a sedimentary basin containing several structural highs, graben, and sub-basins (Skogseid et al., 1992). The Vøring Escarpment and the Vøring Marginal High bound the Vøring Basin in the west, whilst the Nordland Ridge and Trøndelag Platform bound the basin to the east (Brekke, 2000). The Fles Fault Complex and the Bivrost Lineament to the north and the Jan Mayen Lineament to the south also delimit the Vøring Basin (Blystad et al., 1995; Travis et al., 1995; Brekke, 2000). Other critical structural boundaries within the Vøring Basin are the Surt Lineament, the Rym

Fault Zone, and other NW-SE trending lineaments that parallel the Bivrost and Jan Mayen Lineaments (Blystad et al., 1995; Travis et al., 1995; Brekke, 2000).

The geodynamic evolution of the Mid-Norwegian continental margin relates to the tectonic evolution of the Vøring Basin, which hosts a Late Palaeozoic to Cenozoic sedimentary sequence across 150,000 km^2 (Bukovics and Ziegler, 1985). Brekke et al. (1999) identified three periods of rifting along the Mid-Norwegian continental margin occurring in the Carboniferous to Permian, Late-Jurassic to Early Cretaceous, and the Late Cretaceous to Early Eocene. Although the first two extensional phases affect the entire Vøring Basin, they were particularly centered in the eastern Vøring Basin. Older Paleozoic structures were reactivated during these events and are present as rotated fault blocks (Eldholm et al., 1989; Skogseid et al., 1992).

The extensional regime during the Late Jurassic-Early Cretaceous produced syn-tectonic listric faulting in the basin (Skogseid et al., 1992). The Late Jurassic-Early Cretaceous evolution of the study area is recorded by the Nise Formation, which is the oldest formation intersected by borehole 6701/6-1 (Figures 1c, 2 and 3). The Nise Formation is dominated by non-calcareous mudstones deposited in open marine environments (Figures 2 and 3; Dalland et al., 1988). Other rock types within the Nise Formation are mudstones with subordinate siltstones, sandstones, and occasional carbonate stringers (Dalland et al., 1988; Omosanya et al., 2018). In the study area, the Nise Formation is highly deformed by syn-tectonic listric faults.

In the Late Paleocene, magmatism led to the emplacement of sills within the Nise Formation and extrusion of flood basalts onto Cretaceous (and earlier) formations in the study area (Eldholm et al., 1989; Skogseid et al., 1992; Omosanya et al., 2018). The last phase of continental separation between Norway and East Greenland occurred in the Late Cretaceous to Early Eocene and was restricted to the central and western parts of the Vøring Basin. The basin was regionally a deep marine environment at this time, which led to the deposition of dark grey to brown claystones with minor sandstones and limestones, i.e. the Tang Formation (Figures 2 and 3; Dalland et al., 1988).

In the Late Eocene to Oligocene, the Brygge Formation was deposited in the Vøring Basin includes claystone with stringers of sandstone, siltstone, limestone and marl (Figures 2 and 3; Deegan and Scull, 1977; Dalland et al., 1988). In some parts of the Vøring Basin, the Brygge Formation is noted to consist predominantly of ooze sediment (Vogt, 1997; Omosanya et al., 2018). During this period, regional NW-SE compression reactivated and inverted some of the pre-existing normal faults, resulting in folding of hanging wall strata (e.g. Figures 1c and 2;

Faleide et al., 1988; Berggren et al., 1995; Lundin and Doré, 2002; Mjelde et al., 2003). Sills continued to be emplaced into the Cenozoic succession during the Late Eocene to Oligocene and periodically interacted with a complex array of normal and inverted faults (Hansen, 2004; Hansen and Cartwright, 2006a, b). In addition to the tectonic faults, radial and polygonal faults are also documented in the Vøring Basin and likely formed in the Micoene (Omosanya et al., 2018). Consequently, the Miocene to Pliocene Kai Formation in the study area is less affected by deep-seated faults but influenced by the polygonal faults. The Kai Formation is comprised of alternating claystone, siltstone and sandstone with limestone stringers that were deposited in marine environments (Dalland et al., 1988; Eidvin et al., 1998).

Throughout the Pliocene-Pleistocene, the Vøring Basin and the Norwegian mainland experienced intense uplift and erosion, which favoured the deposition of sedimentary strata towards the shelf edge (Skogseid et al., 1992). Uplift and glaciation indicate that deep glacial erosion had removed 1-2 km sedimentary cover from the Norwegian onshore. The product of this erosional event was deposited as a wedge of glaciomarine sediments or formations (Riis and Fjeldskaar, 1992; Eidvin et al., 2014), which consists mainly of claystone, siltstone and sand, with occasional very coarse clastics appearing at its upper part, known as the Naust Formation (Dalland et al., 1988).

3. Dataset and methods

The primary dataset used for this study are high-quality, three-dimensional (3-D) seismic data and wireline logs from borehole 6706/6-1 (Figures 1 and 3). The 3-D seismic dataset covers an area of approximately 1998 km^2 in the northern Vøring Basin, where the maximum water depth is ~1298 m. The survey has a vertical sampling interval of 2 ms two-way travel time (TWTT), a maximum vertical length of 8000 ms TWTT, with bin spacing for inline (north-south direction) and crossline (east-west direction) of 25 m and 12.5 m, respectively. The seismic data is zero-phased and displayed in SEG (Society for Exploration Geophysicist) normal polarity convention i.e. an increase in acoustic impedance with depth corresponds to a peak (blue reflection) whilst a decreasing acoustic impedance with depth corresponds to a trough (red reflection). In addition to the 3D seismic data, a 2D seismic line (Figures 1c and 2) was used to project the location of the study area within the regional structural framework of the Vøring Basin. Borehole 6706/6-1 was drilled as a frontier well to test the hydrocarbon potential of a Cretaceous prospect in the Vøring Basin, with a total depth of 3451 m (RKB).

The vertical resolution or limit of separability (ʎ/4, where ʎ is the wavelength) determines whether reflections emanating from the top and base of a bed, or structure (e.g. a sill), can be distinguished and used to estimate thickness (Sheriff and Geldart, 1995). The vertical resolution of the sedimentary sequence within our interval of interest is c. 18 m, which was calculated using a dominant frequency of c. 28 Hz and an average velocity of 2000 m/s based on borehole data. We have no velocity information for the sills, but assuming their seismic velocity is 5550±555 m/s, consistent with intrusions examined elsewhere along the Norwegian margin (e.g.Skogly, 1998; Planke et al., 2005), we expect their vertical resolution to be c. 50±5 m. Most sills in the study area are, however, expressed as tuned reflection packages, whereby reflections from their upper and lower contacts interfere on their return to the surface, meaning their thickness is <50±5 m (e.g. Sheriff and Geldart, 1995; Smallwood and Maresh, 2002; Brown, 2004; Hansen et al., 2008; Eide et al., 2017; Schofield et al., 2017; Mark et al., 2018). The detection limit, or limit of visibility (λ/30), for the sills is c. 6–7 m. Hence, intrusions with thicknesses below this value may be detected in the seismic data but are likely to be difficult to differentiate from the surrounding strata (Eide et al., 2017; Schofield et al., 2017). The detection limit for the sedimentary sequence is c. 2 m.

Seismic interpretation involved mapping of five stratigraphic units, 12 magmatic sills, and 64 faults. The stratigraphic units were identified and tied to five well tops in borehole 6706/6-1 using integrated seismic well tie, which allowed formation age to be constrained (Figure 3). The five mapped horizons are the upper Cretaceous Nise Formation (NS), the Late Palaeocene to Early Miocene Tang Formation (TG), the Late Eocene to Oligocene Brygge Formation (BG), the Miocene to Pliocene Kai Formation (KI) and the Late Pliocene-Quaternary Naust Formation (NA). Magmatic sills were interpreted based on their amplitude character, geometry, and lateral continuity within the host-rock strata (Planke et al., 2005). For example, within seismic reflection data, sills normally show high-amplitudes relative to the host sedimentary strata, local transgression across stratigraphic levels, and/or restricted lateral continuity (e.g. Planke et al., 2000; Smallwood and Maresh, 2002).

Faults were mapped every c. 25 m – 125 m along lines perpendicular to fault strike and identified on seismic sections by fault-horizon cutoffs (Figure 4a). The displacement plots used the offset of the top formation (i.e Tang and Nise Formations) to the sill to evaluate the D-x. Accurate mapping of faults was aided by using variance slices to map the fault trace in plan view (Figure 4b). The variance seismic attribute represents trace-to-trace variability within specific sample interval and hence can indicate changes in acoustic impedance and reflection termination patterns (Figure 4b; Brown, 2004); variance was also used to distinguish high-amplitude reflections related magmatic sills from homogeneous sandstones beneath the Nise Formation (Figures 4a and 4b). Fault displacements were assumed to be dip-slip. Fault displacement data were collected by measuring the vertical separation (i.e. throw) and horizontal separation (i.e. heave) between footwall and hanging wall cut-offs of interpreted horizons on seismic sections oriented perpendicular to the fault strike (Figures 4c and 4d). In addition, we emphasize that the sills here are tuned reflections and, thus, their top and bases cannot be distinguished; this is particularly relevant considering that the offset between the sill portion in the hanging wall and footwall is an apparent displacement.

4. Overview of interpreted stratigraphic units

The upper Cretaceous Top Nise (NS) structure map (Figure 5a) best illustrates the kinematic style of fault networks within the study area, as it depicts deformation associated with Late Cretaceous to the Early Eocene extensional system in the Mid-Norwegian continental margin. Here on the NS map, the influence of E-W and N-S oriented faults are manifested as fault scarps. On seismic sections, the NS includes low to moderate amplitude and faulted reflections. Overlying the NS is the Late Palaeocene to Early Miocene Tang Formation (TG) (Figure 5b), which consists of low to moderate amplitude reflections (Figures 1c, 3, 6a, 6b and 6c). The Tang Formation contains of several complex structures, such as growth of an anticline, formed in response to tectonic inversion along faults (Figurse 4b and 5a). The Late Eocene to Oligocene Brygge Formation (BG) (Figure 5c) includes continuous, low to high amplitude reflections (Figures 1c, 3, 6a and 6b). Hydrothermal vents and polygonal faults are common within the Tang and Brygge Formations (Figures 1c, 3 and 6c).

The Miocene to Pliocene Kai Formation (KI) contains continuous and low to high amplitude reflections (Figures 1c, 3, 6a and 6c). The time structure map of the Kai Formation shows evidence for a NW-SE (N150°E) oriented fold (Figure 5d), interpreted as a manifestation of an Oligocene compressional event that caused tectonic inversion in the study area (Omosanya et al., 2017). Inversion is evidenced by reflections showing snake-head geometries (Figure 1c; Omosanya et al., 2017a), which are secondary contractional deformation structures/folds common in inverted rift basins and are formed by reverse reactivation of faults (Allmendinger, 1998). Evidence for this inversion-related fold is further reflected in the structural map of the youngest and uppermost formation i.e. the Late Pliocene-Quaternary Naust Formation (Figures 1c and 5e). The Naust Formation includes continuous and moderate to high amplitude reflections at its upper part and base (Figures 1c, 3, 6a and 6b). At the SE part of the study area, the base of the Naust Formation is strongly affected by folds related to the pronounced snake-head structures (Figure 1c).

4.1 Seismic interpretation of magmatic sills

The morphometry data for the 12 interpreted sills are presented in Table 1. Sills have long axes that are broadly oriented in SE-NW or NE-SW directions and occur within the interval between -2500 ms to -6000 ms TWTT (Figures 6 and 7, Table 1). Sill geometries include concave-upwards saucer-shape (e.g. Sill-B; Figure 7b), transgressive (e.g. Sill-G; Figure 7g), and strata-concordant (e.g. Sill-K; Figure 7k) (see Planke et al., 2005). Saucer-shaped sills are characterised by an inner, broadly strata-concordant sill encompassed by an inclined sheet, which may feed a stratigraphically higher outer sill (e.g. Sill-A; Figure 7a) (Thomson and Hutton, 2004). In several places, the transgressive limbs of sills or parts of inclined sheets appear to coincide with fault planes (e.g. Sill-D; Figure 7d). These intrusive portions coincident with fault planes occasionally link to stratigraphically higher sills in the footwall (Figure 7e). The main sill-complex (Figure 1c) and local saucer-shaped sill (i.e., Sill-H; Figures 7h and 8) are directly overlain by dome-shaped folds (i.e., the lateral limits of each are broadly coincident).

The sill complex (Figures 1c and 2) is interpreted to have influenced the growth of a large asymmetric forced fold in the basin (see also Omosanya et al., 2017) whilst the presence of the local sill (i.e. saucer-shaped sill) presumably allowed symmetrical fold to be formed in the their overburden (Figures 7h and 8). These forced folds are interpreted to be post depositional because they are onlapped by Late Eocene to Oligocene strata of the Brygge Formation (Figures 1c, 2 and 7h). Besides magmatic impact on the regional forced fold, tectonic influence might also have significant role during subsequent modulation of the large fold. More so, other onlap reflections at the Brygge Formation level (Figure 2) might suggest later influence of tectonic inversion on the large fold. As for the saucer-shaped sill in Figures 7h and 8, the overlying dome-shaped fold developed at the Top Tang Formation and onlapped by overlying strata of the Brygge Formation (Figures 7h and 9). More so, the lateral limits of this fold are coincident with the lateral terminations of the sill (Figures 7h, 8 and 9).

Saucer-shaped sills cover an area ranging from 6 km^2 – 113 km^2 and have lengths of 12 km – 55 km (Table 1). Sills with broadly radially symmetrical forms (e.g. Sill-H and Sill-I) have limited distribution, with areas <10 km^2 and lengths <15 km (Table 1). Transgressive sills have areas of 156 – 180 km^2 with lengths of 58 – 66 km, whilst strata-concordant sills have areas of up to ~42 km^2 and lengths of ~35 km (Table 1). Based on their relative depths, we classify the sills into three types. Shallow sills that are located at depths less than -3000 ms TWTT, intermediate sills range from -3000 to -5000 ms TWTT and deep sills at depths higher than -5000 ms TWTT. The shallow sills have areas ranging from 6 km^2 – 42 km^2 and lengths of 12 km - 35 km (Table 1). The area coverages and lengths of the deeper sills range from 113 km^2 – 156 km^2 and 55 km – 58 km, respectively (Table 1). Intermediate sills have length and area coverage of 19 km – 180 km and 19 km^2 – 66 km^2 (Table 1).

4.2 Interpretation of tectonic faults in the study area

The study area contains tectonic, polygonal, and radial faults (Figures 1c and 6). Of interest here are the tectonic normal faults, which can reach about 28 km long in plan-view (Figure 5). These normal faults dominantly have E-W trends, with mean direction = N87°E, and varied dips, with mean = 28° (Figure 10a). Northerly dipping faults, such as F81 and F84 (Figure 12, 12c and 12 d), have smaller fault displacements (5-279 m) and lengths (2,200- 2,700 m) compared to southerly dipping faults, which have displacements and lengths of up to 778 m and 17,000 m, respectively (Figures 13e and 13g). In general, the tectonic normal faults in the study area have displacement values that range from <10–1,000 m and length from 1,000–30,000 m (Figure 10b). Plots of maximum displacement against fault length for all the faults between the Tang and Nise Formations display multiple areas of high-displacement, locally marked by bell-shaped curves, separated by displacement minima (Figures 14 and 15). Although the majority of the faults display a normal sense of motion and are commonly basement-rooted, with their upper tips located in the Eocene-Oligocene Kai Formation (Figures 1c and 6b), some inverted faults are observed in the northern part of the study area (Figures 1c and 6a). These inverted faults are constrained to the Late Cretaceous and Oligocene strata (Figures 1c and 6a).

4.3 Interpretation of fault-sill intersection geometries

To explain the intricacy of fault-sill interaction, we use geometrical measurements at the fault-sill interfaces to demonstrate their exclusive characters (Table 2). The five intersection geometries types observed here are (Table 2): Type 1a, e.g. Sill-A, Sill-B and Sill-C; Type 1b, e.g. Sill-D and Sill-E; Type 2, e.g. Sill-F and Sill-G; Type 3, e.g. Sill-H and Sill-I; and Type 4, e.g. Sill-J, Sill-K and Sill-L (Figures 6b, 6c and 7). The difference between Type 1a, 1b and 2 is related to the ability of the sill to step up younger stratigraphic layers by transecting the fault plane from the hanging wall side to the footwall. For Type 1a, the sills transgress along the fault plane without intruding into the footwall side (e.g. Figures 7b and 7c; Table 2), whilst Type 1b and 2 have sills intersecting the fault planes and intruding across to the footwall side (e.g. Figures 6e and 6f; Table 2). Type 3 and 4 interactions involve sills that intersect several faults (e.g. Figures 7h and 7j; Table 2).

Geometrically, fault orientations for Type 1 to 3 are similar (Figure 10, Table 2). Here, the faults strike typically ranges from N170°E to N185°E with a mean value of about N184°E and angle of dip ranges from 20° to 45°. In terms of the associated fault-sill interaction types, Types 1 to 3 are usually associated with normal tectonic faults (Figures 6b, 6c and 7h; Table 2). For Type 4, fault strikes can range from N130°E to N200°E and with the angle of dip from 20° to 65°.

Type 4 fault-sill interfaces are usually connected to polygonal faults and generally display structural elements such as apparent steps or bridges (Figure 7j).

For detailed measurements of the fault-sill intersection, we examine the interaction style for Sill-A (Type 1a) and Sill-F (Type 2). We describe Sill A as a saucer-shaped sill that covers c. 113 km^2 (Figures 5e, 6b and 7a; Table 1), with an inclined limb that coincides with fault F60 vertically for up to ~600 ms TWTT (Figure 12a). Sill-A is associated with four key normal faults, i.e. F60, F61, F62 and F64 (Figures 9d, 9e, 12a and 12b). These faults were selected due to their vertical extension through the Naust Formation (NA) to Sill-A (Figures 8a-e), allowing displacement to be measured (Figure 14). Predominantly, all faults have strikes that range from N177°E to N191°E with a mean value around N184°E and dip of 29 °south (Figure 12f). The four faults are observed to extend from the Eocene formation (BG) to the basement (Figure 11a-10c) except for fault F64 (Figure 11c) which has an upper tip within the Paleocene Formation (TG). A series of steps are recognized within Sill-A, which are oriented E-W (Figure 11d), broadly parallel to fault strike and have a height range of 10 m to 30 m (Figure 11g).

Sill-F is situated between the Tang Formation (TG) and Nise Formation (NS) at a depth range of -3069 ms to -3727 ms TWTT in the southeastern part of the study area (e.g. Figure 5e). Sill-F is transgresive, covers an area of c. 179 km^2 and is intersected by six normal faults, i.e. F74, F75, F76, F78, F82 and F84 (Figures 9d, 9e, 10c and 10d). The displacement plots in Figure 15 used the offset of the Tang Formation (TG) as Sill-F is restricted to this interval (Figures 9b and 9c), allowing D-x to be evaluated. Predominantly faults have strikes range from N130°E to N191°E with a mean value about N163.6°E-striking and 42.28°-dipping to the northeastwards (Figure 12f). In seismic data, Sill-F is inclined to fault F74 vertically for up to 225 ms TWTT (Figure 12c). Furthermore, five steps were observed within the Sill-F, ranging from 26 m to 65 m in height (Figure 12g) oriented NW-SE and E-W (Figure 12d).

4.4 Relationship between sill intrusion on fault displacement.

The D-x profiles, measured along the Top Nise Formation, for the four main faults associated with Sill-A are complex, showing fault displacement is segmented (i.e. 3–5 segments) with displacement maxima bound by prominent displacement minima (Figure 14). These fault segments have maximum displacement (d_{max}) that range from ~115–600 m (Figure 14). Faults F60 (456 m d_{max}), F61 (116 m d_{max}), F62 (581 m d_{max}) and F64 (328 m d_{max}) are intruded by sills towards their lower tips (Figures 8 and 10). In the case of F60, the fault segment with the maximum displacement, has the tallest sill step (~26 m) at its lower tip (Figures 8d and 8g), whilst gap between the point of measured d_{max} and the fault-sill interfaces is from ~41 m to 187 m for Sill A (Figure 14a). On the D-z plots, displacement for all four main faults ranges from

~24 m up to 187 m (Figure 16a). Fault displacement generally decreases gently toward the basal tip with gradients of 38 (Figure 16a). Fault-sill junctions are observed ~1 s TWTT below the maximum displacement of two faults (i.e. F60 and F64), which occur at depths below -3500 ms TWTT (Figure 16a). Overall, all the faults for Sill A have D-z profiles showing C-type vertical displacement profiles (Figure 16a;e.g. Baudon and Cartwright, 2008).

For Sill-F, the displacement plots for F79 and F80 are not included as they show little or no impact on the geometry of Sill-F (Figures 11c and 11d). The seven main faults associated with Sill-F display segmented D-x profiles, where displacement maximima are separated by displacement minima, indicating the faults grew view linkage between discrete slip surfaces (Figure 15). These faults have four to eleven lateral segments (Figure 15). Lateral segments on these faults have displacement maxima that range from ~60–220 m (Figure 15); e.g. F74 (218 m), F75 (210 m), F81 (77.64 m), F82 (151 m), F84 (64 m). In a similar way as faults that interact with Sill A, the faults associated with Sill F contain segments that are intruded towards their lower tips (Figure 15). Displacement maxima occur on these segments (e.g. F81, F82 and F84) above the sills (Figure 15). The distance between the point of measured Dmax and the sill-fault interfaces range from ~26-151 m (Figure 16b). Unlike Sill A, steps beneath these segments (Figure 12g) have heights that could range from ~26 m (S2) to ~58 m (S5). The D-z plots (Figure 16b) for the seven faults all have a C-type morphology. All the D-z plots have their points of d_{max} above the location of sill intrusion (appear mostly in the Brygge Formation) (Figure 16b).

5. Timing, style and emplacement of magmatic sills into pre-existing faults

Evidence concerning the tectonic evolution affecting the study area documented in fault patterns, implies a complex fault timing, structure, and growth (Figures 1c, 4 and 5). A series of relative E-W-trending faults, which are basement-rooted with their upper tips within the Eocene-Oligocene formation, are interpreted as being of Early Paleocene to Early Eocene age (Figures 1c and 5) and likely correspond to a period of extension between Norwegian-Greenland Seas (see Malthe-Sorensson et al., 2004; Planke et al., 2005; Hansen and Cartwright, 2006b; Svensen et al., 2010; Omosanya et al., 2017). Seismic interpretation indicates growth of an inversion anticline, which produced the E-W trending hanging wall fold within Oligocene strata (Figure 6a). These correspond to a compressional event that occurred in Late Eocene to Oligocene or younger (Omosanya et al., 2017).

Although we have no direct dating evidence for the imaged sills, one saucer-shaped sill is directly overlain by a dome-shaped fold, which we interpret to have formed in response to roof uplift during magma emplacement (e.g. Hansen and Cartwright, 2006a; Magee et al., 2013b);

i.e. it is an intrusion-induced forced fold (Figures 4c,7h and 8). The top of this intrusion-induced forced fold occurs at the Top Tang formation and is onlapped by Late Eocene to Oligocene strata of the Brygge Formation (Figures 1c, 2 and 7h), indicating fold growth and, thereby, sill emplacement occurred in the Eocene. We consider this age as a plausible estimate for the entire sill-complex, which cross-cuts and is thus younger than Late Cretaceous to Early Eocene strata (Figures 1c, 2 and 8). Sill emplacement thus likely post-dates normal fault formation in the study area, but perhaps not inversion.

We observe that sills coincide with and appear to intrude normal faults as they transgress to higher stratigraphic levels. We consider four potential mechanisms that may promote sills to intrude the fault planes: (1) along-strike variations in fault dip, with intruded fault portions perhaps being more favourably oriented with respect to σ_3 and thus able to 'open' during intrusion; (2) changes in fault rock properties that may affect the rheological behaviour of the fault rock and favour intrusion; (3) juxtaposition of rocks across the fault plane with different stiffnesses that may deflect propagating sheets; and/or (4) a localized rotation of σ_3 perpendicular to the fault plane (Valentine and Krogh, 2006; Bédard et al., 2012; Magee et al., 2013a). Where sills exploit faults, the dip of the fault plane is typically <30° (Figure 13). Given observed tectonic normal faults have dip angles ranging from 20°-45°, but not all the faults, or even portions of faults, with low dips have acted as magma pathways, it seems unlikely that changes in fault dip accounts for the observed sill emplacement patterns (Figures 8f, 9f and 10).

As faults grow and accrue more displacement, associated fault damage zones cany increase in size, localised deformation (e.g. fracturing) may become more intense, and fault rocks could fine, potentially leading to the fault zone becoming 'weak' and conducive to fluid flow (e.g. Kim et al., 2004; Faulkner et al., 2010). It may be expected that sill transgression along faults preterentially occurs along portions of the fault plane weakened by increased slip (Magee et al., 2013a). If weakened fault rocks and/or damage zones do allow intrusion, we may thus expect a correlation between fault-sill interactions and fault displacement. The D-z plots generally have C-type morphologies, consistent with nucleation of isolated faults and and growth by radial tip-line propagation (Watterson, 1986; Barnett et al., 1987; Walsh and Watterson, 1991; Walsh et al., 2003; Kim and Sanderson, 2005). The occurrence of multiple displacement maxima along fault strike suggest faults grew laterally via linkage of initially isolated fault segments (Peacock and Sanderson, 1991; Cartwright et al., 1995; Gawthorpe and Leeder, 2000; Walsh et al., 2003; Kim and Sanderson, 2005; Mattos et al., 2015). Although the height of the sill portion that intrudes faults varies along fault length (Figures 13 and 14), there is no apparent correlation between the amount of displacement on each segment and sill height; only for F75 and F82 does the maximum sill height occur in the segment containing the fault d_{max} (Figures 14b and 14f). Our results indicate variations in fault displacement had little linfluence on where sills intruded, implying supposedly weak fault zones/rocks are not preferentially intruded (cf. Magee et al., 2013c).

Changes in lithology across stratigraphic levels may also be critical for growth and emplacement of sill within a fault. Pollard and Johnson (1973); Kavanagh et al. (2006); Zhang et al. (2007) and references therein documented that a dyke reaching a boundary between two units will deflect either because the unit above is too stiff to intrude or because the boundary itself is weak and relatively easy to intrude. Using this analog, whilst the boundaries between lithological units may be exploited by a sill (e.g. Pollard et al., 1975; Gudmundsson, 2009), if a fault offsets and juxtaposes the intruded boundary against a 'stronger' unit, we suggest the sill may be deflected up the fault.

We favour that the fourth mechanism, i.e. a local re-orientation of σ_3, likely controlled sill emplacement and fault-sill interactions (Magee et al., 2013c). Importantly, intrusive steps away from fault planes are oriented parallel to the fault strike, suggesting sills in the hanging wall intruded along fault strike (Figures 11 and 12). Magee et al. (2013c) suggested that roof uplift instigated by sills in the hanging wall, which intrude towards or parallel to faults planes, could locally open faults by reorienting σ_3 and allowing sills to 'step up' the fault planes. Where sills approach a fault from the footwall side, uplift of the sill acts to 'pin' the fault, keeping it closed and inhibiting intrusion (Magee et al., 2013c). Whilst such a local re-orientation of σ_3, controlled by the relative position of the intruding sill to the fault plane, can explain how magma intrudes up a fault, the question remains as to why some sill portions intrude further up fault planes than others (i.e. to produce the different fault-sill interaction types observed).

5.1 Implications for structural compartmentalization in basins and outcrop-scale studies

1- Reservoir compartmentalization

The emplacement of sills within fault planes could further lead to isolation of fluid pathway and result in reduced host rock permeability (see Holford et al., 2013). Such isolated compartments may impact the efficiency of hydrocarbon mobilization out of source rocks and into reservoirs (Holford et al., 2013; Schofield et al., 2017). Hence, the geometric relationship provided here are relevant for assesing impact of sill intrusion on fault seal integrity.

2- Implications for outcrop-scale studies

Only a few outcrop-scale studies of fault-sill interactions have been published (e.g., Bédard et al., 2012; Walker, 2016; Stephens et al., 2017) show sill segments relationship with thrust fault in the Faroe Islands, European Atlantic passive margin. The work signified the extent to which initial sill propagation through a fault system is associated with the thickness of the host rock. In addition, Bédard et al. (2012) have also revealed that the sill-dominated feeder system in the Franklin Sill, Victoria Island, Canada is controlled by faults, allowing magma ascent to higher stratigraphic levels. In particular, Stephens et al. (2017) show that intrusion geometry in the Loch Scridain Sill Complex (Isle of Mull, UK) is primarily controlled by far-field stresses with local and secondary control associated with layering and pre-existing structures. The limitation in outcrop observation of fault-sill interactions is largely due to the fact most these interactions are deeply buried. Hence, the geometric and quantitative interpretation/data from this study can give important insight in determining fault-sill interactions and its wider understanding of sill evolution, interactions, mechanisms and controls. This is important to give better insight of sedimentary or volcanic rift basins evolution and to allow hydrocarbon and resource assessment related to these settings.

6. Conclusions

This work has used 3-D dimensional seismic reflection data to evaluate fault-sill interactions and mechanisms controlling sill intrusion along fault planes. Five types of fault-sill interaction geometries have been recognized based on three-dimensional (3-D) seismic interpretation from the Naglfar Dome, Vøring Basin, Mid-Norwegian continental margin. The pre-existing faults often have an association with extensional tectonic activity in Early Paleocene to Early Eocene during the opening of the Norwegian-Greenland Seas and a Late Eocene to Oligocene compressional event that caused tectonic inversion in the study area. The complex interaction between the sills and pre-existing faults across the Late Cretaceous to Early Eocene formations indicates that sill emplacement occurred in the Eocene. We suggest flow direction relative to the fault plane orientation eventually enables sills to re-direct their propagation paths into pre-existing faults. We note fault displacement has no influence on sill intrusion in the study area. We conclude that magma transport within the fault plane occurred at an orientation perpendicular to the least compressive stress (σ_3).

Acknowledgments

Einstein is grateful to ARCEX for sponsoring his position at NTNU (Norwegian University of Science and Technology). This work was sponsored by the ARCEx project (Research Centre for Arctic Petroleum Exploration) which is funded by the Research Council of Norway (grant number 228107) together with ten academic and nine industry partners. We also acknowledge the Norwegian Petroleum Directorate (NPD) for graciously granting access to the borehole data used in this research (www.npd.no). Schlumberger for the provision of Petrel® and Petrel-ready project for seismic interpretation and Midland Valley Move® for the provision of the academic license for multi-structural analysis to NTNU (Norwegian University of Science and Technology). We thank Nick Schofield and David K. Muirhead for their outstanding and constructive reviews. We are also grateful to the editor C. W. Passchier for his contributions during the review process.

References

Allmendinger, R.W., 1998. Inverse and forward numerical modeling of trishear fault-propagation folds. Tectonics 17, 640-656.

Barnett, J.A., Mortimer, J., Rippon, J.H., Walsh, J.J., Watterson, J., 1987. Displacement geometry in the volume containing a single normal fault. AAPG Bulletin 71, 925-937.

Baudon, C., Cartwright, J., 2008. The kinematics of reactivation of normal faults using high resolution throw mapping. Journal of Structural Geology 30, 1072-1084.

Bédard, J., Naslund, H., Nabelek, P., Winpenny, A., Hryciuk, M., Macdonald, W., Hayes, B., Steigerwaldt, K., Hadlari, T., Rainbird, R., 2012. Fault-mediated melt ascent in a Neoproterozoic continental flood basalt province, the Franklin sills, Victoria Island, Canada. Geological Society of America Bulletin 124, 723-736.

Berggren, W.A., Kent, D.V., Swisher, I.I.I.C.C., Aubry, M.-P., 1995. A Revised Cenozoic Geochronology and Chronostratigraphy, in: Berggren, W.A., Kent, D.V., Aubry, M.-P., Hardenbol, J. (Eds.), Geochronology, Time Scales and Global Stratigraphic Correlation. SEPM Society for Sedimentary Geology.

Blystad, P., Brekke, H., Færseth, R.B., Larsen, B.T., Skogseid, J., Tærudbakken, B., 1995. Structural elements of the Norwegian continental shelf. Part II. The Norwegian Sea Region., NPD, Norwegian Petroleum Directorate, Bulletin 8, pp. 1-45.

Brekke, H., Dahlgren, S., Nyland, B., Magnus, C., 1999. The prospectivity of the Voring and More basins on the Norwegian Sea continental margin. Petroleum Geology Conference Series 14, 261-274.

Brekke, H., 2000. The tectonic evolution of the Norwegian Sea Continental Margin with emphasis on the Voring and More Basins. Geological Society, London, Special Publications 167, 327-378.

Brown, A., 2004. Interpretation of three-dimensional seismic data: The American Association of Petroleum Geologists and the Society of Exploration Geophysicists. Tulsa, OK 535.

Bukovics, C., Ziegler, P.A., 1985. Tectonic development of the Mid-Norway continental margin. Marine and Petroleum Geology 2, 2-22.

Cartwright, J., Hansen, D.M., 2006. Magma transport through the crust via interconnected sill complexes. Geology 34, 929-932.

Cartwright, J.A., Trudgill, B.D., Mansfield, C.S., 1995. Fault growth by segment linkage: an explanation for scatter in maximum displacement and trace length data from the Canyonlands Grabens of SE Utah. Journal of Structural Geology 17, 1319-1326.

Dalland, a., Worsley, D., Ofstad, K., 1988. A lithostratigraphic scheme for the Mesozoic and Cenozoic succession offshore mid- and northern Norway, Norwegian Petroleum Directorate Bulletin, p. 65.

Deegan, C.t., Scull, B.J., 1977. A standard lithostratigraphic nomenclature for the Central and Northern North Sea. HMSO.

Delaney, P.T., Pollard, D.D., Ziony, J.I., McKee, E.H., 1986. Field relations between dikes and joints: emplacement processes and paleostress analysis. Journal of Geophysical Research: Solid Earth 91, 4920-4938.

Eide, C.H., Schofield, N., Lecomte, I., Buckley, S.J., Howell, J.A., 2017. Seismic interpretation of sill complexes in sedimentary basins: implications for the sub-sill imaging problem. Journal of the Geological Society, jgs2017-2096.

Eidvin, T., Brekke, H., Riis, F., Renshaw, D.K., 1998. Cenozoic stratigraphy of the Norwegian Sea continental shelf 64degreesN-68degreesN. Norsk Geologisk Tidskrift 78, 125-151.

Eidvin, T., Riis, F., Rasmussen, E.S., 2014. Oligocene to Lower Pliocene deposits of the Norwegian continental shelf, Norwegian Sea, Svalbard, Denmark and their relation to the uplift of Fennoscandia: A synthesis. Marine and Petroleum Geology 56, 184-221.

Eldholm, O., Thiede, J., Taylor, E., 1989. Evolution of the Vøring Volcanic Margin, Proceedings of the Ocean Drilling Program, 104 Scientific Results, pp. 1033-1065.

Faleide, J.I., Myhre, A.M., Eldholm, O., 1988. Early Tertiary volcanism at the western Barents Sea margin. Geological Society, London, Special Publications 39, 135-146.

Faulkner, D., Jackson, C., Lunn, R., Schlische, R., Shipton, Z., Wibberley, C., Withjack, M., 2010. A review of recent developments concerning the structure, mechanics and fluid flow properties of fault zones. Journal of Structural Geology 32, 1557-1575.

Gawthorpe, R., Leeder, M., 2000. Tectono-sedimentary evolution of active extensional basins. Basin Research 12, 195-218.

Gudmundsson, A., 2009. Initiation of rift-zone crustal magma chambers through the deflection of dykes into sills at layer contacts, EGU General Assembly Conference Abstracts, p. 4248.

Hansen, D.M., 2004. 3D seismic characterisation of igneous sill complexes in sedimentary basins: North-East Atlantic Margin, p. 451.

Hansen, D.M., Cartwright, J., 2006a. The three-dimensional geometry and growth of forced folds above saucer-shaped igneous sills. Journal of Structural Geology 28, 1520-1535.

Hansen, D.M., Cartwright, J., 2006b. The morphology of intrusion-related vent structures and their implications for constraining the timing of intrusive events along the NE Atlantic margin. Journal of the Geological Society 163, 789-800.

Hansen, D.M., Redfern, J., Federici, F., Di Biase, D., Bertozzi, G., 2008. Miocene igneous activity in the Northern Subbasin, offshore Senegal, NW Africa. Marine and Petroleum Geology 25, 1-15.

Holford, S., Schofield, N., Jackson, C., Magee, C., Green, P., Duddy, I., 2013. Impacts of igneous intrusions on source and reservoir potential in prospective sedimentary basins along the Western Australian continental margin, West Australian Basins Symposium. Proceedings of the Petroleum Exploration Society of Australia Symposium, Perth, WA, pp. 1-12.

Kavanagh, J.L., Menand, T., Sparks, R.S.J., 2006. An experimental investigation of sill formation and propagation in layered elastic media. Earth and Planetary Science Letters 245, 799-813.

Kim, Y.-S., Peacock, D.C., Sanderson, D.J., 2004. Fault damage zones. Journal of structural geology 26, 503-517.

Kim, Y.-S., Sanderson, D.J., 2005. The relationship between displacement and length of faults: a review. Earth-Science Reviews 68, 317-334.

Lundin, E., Doré, A., 2002. Mid-Cenozoic post-breakup deformation in the ‘passive’margins bordering the Norwegian–Greenland Sea. Marine and Petroleum Geology 19, 79-93.

Magee, C., Jackson, C.A.-L., Schofield, N., 2013a. The influence of normal fault geometry on igneous sill emplacement and morphology. Geology 41, 407-410.

Magee, C., Hunt-Stewart, E., Jackson, C.A.L., 2013b. Volcano growth mechanisms and the role of sub-volcanic intrusions: Insights from 2D seismic reflection data. Earth and Planetary Science Letters 373, 41-53.

Magee, C., Jackson, C.A.L., Schofield, N., 2013c. Interaction between Faults and Igneous Intrusions in Sedimentary Basins: Insights from 3D Seismic Reflection Data*, AAPG International Conference and Exhibition. AAPG©2012, Singapore.

Malthe-Sorensson, A., Planke, S., Svensen, H., Jamtveit, B., 2004. Formation of saucer-shaped sills. 215-227.

Mark, N., Schofield, N., Pugliese, S., Watson, D., Holford, S., Muirhead, D., Brown, R., Healy, D., 2018. Igneous intrusions in the Faroe Shetland basin and their implications for hydrocarbon exploration; new insights from well and seismic data. Marine and Petroleum Geology 92, 733-753.

Mattos, N.H., Alves, T.M., Omosanya, K.O., 2015. Crestal fault geometries reveal late halokinesis and collapse of the Samson Dome, Northern Norway: Implications for petroleum systems in the Barents Sea. Tectonophysics.

Mcclay, K.R., Ellis, P.G., 1987. Geology Geometries of extensional fault systems developed in model experiments Geometries of extensional fault systems developed in model experiments. 341-344.

Mjelde, R., Shimamura, H., Kanazawa, T., Kodaira, S., Raum, T., Shiobara, H., 2003. Crustal lineaments, distribution of lower crustal intrusives and structural evolution of the Vøring Margin, NE Atlantic; new insight from wide-angle seismic models. Tectonophysics 369, 199-218.

Omosanya, K.O., Johansen, S.E., Eruteya, O.E., Waldmann, N., 2017. Forced folding and complex overburden deformation associated with magmatic intrusion in the Vøring Basin, offshore Norway. Tectonophysics 706, 14-34.

Omosanya, K.O., Eruteya, O.E., Siregar, E.S., Zieba, K.J., Johansen, S.E., Alves, T.M., Waldmann, N.D., 2018. Three-dimensional (3-D) seismic imaging of conduits and radial faults associated with hydrothermal vent complexes (Vøring Basin, Offshore Norway). Marine Geology 399, 115-134.

Peacock, D., Sanderson, D., 1991. Displacements, segment linkage and relay ramps in normal fault zones. Journal of Structural Geology 13, 721-733.

Planke, S., Symonds, P.A., Alvestad, E., Skogseid, J., 2000. Seismic volcanostratigraphy of large-volume basaltic extrusive complexes on rifted margins. Journal of Geophysical Research: Solid Earth 105, 19335-19351.

Planke, S., Rasmussen, T., Rey, S.S., Myklebust, R., 2005. Seismic characteristics and distribution of volcanic intrusions and hydrothermal vent complexes in the Vøring and Møre basins. Petroleum Geology: North-West Europe and Global Perspectives 6, 833-844.

Pollard, D.D., Johnson, A.M., 1973. Mechanics of growth of some laccolithic intrusions in the Henry Mountains, Utah, II: bending and failure of overburden layers and sill formation. Tectonophysics 18, 311-354.

Pollard, D.D., Muller, O.H., Dockstader, D.R., 1975. The form and growth of fingered sheet intrusions. Bulletin of the Geological Society of America 86, 351-363.

Riis, F., Fjeldskaar, W., 1992. On the magnitude of the Late Tertiary and Quaternary erosion and its significance for the uplift of Scandinavia and the Barents Sea, Structural and Tectonic Modelling and its Application to Petroleum Geology. Elsevier, pp. 163-185.

Schofield, N., Brown, D.J., Magee, C., Stevenson, C.T., 2012. Sill morphology and comparison of brittle and non-brittle emplacement mechanisms. Journal of Structural Geology 169, 127-141.

Schofield, N., Holford, S., Millett, J., Brown, D., Jolley, D., Passey, S.R., Muirhead, D., Grove, C., Magee, C., Murray, J., 2017. Regional magma plumbing and emplacement mechanisms of the Faroe-Shetland Sill Complex: implications for magma transport and petroleum systems within sedimentary basins. Basin Research 29, 41-63.

Sheriff, R.E., Geldart, L.P., 1995. Exploration Seismology, Second Edition.

Skogly, O.P., 1998. Seismic characterization and emplacement of intrusives in the Vøring Basin.

Skogseid, J., Pedersen, T., Eldholm, O., Larsen, B.T., 1992. Tectonism and magmatism during NE Atlantic continental break-up: the Vøring basin. Magmatism and the Causes of Continental Break-up 68, 305-320.

Smallwood, J.R., Maresh, J., 2002. The properties, morphology and distribution of igneous sills: modelling, borehole data and 3D seismic from the Faroe-Shetland area. Geological Society, London, Special Publications 197, 271-306.

Stephens, T.L., Walker, R.J., Healy, D., Bubeck, A., England, R.W., McCaffrey, K.J., 2017. Igneous sills record far-field and near-field stress interactions during volcano construction: Isle of Mull, Scotland. Earth and Planetary Science Letters 478, 159-174.

Svensen, H., Planke, S., Jamtveit, B., Pedersen, T., 2003. Seep carbonate formation controlled by hydrothermal vent complexes: A case study from the Vøring Basin, the Norwegian Sea. Geo-Marine Letters 23, 351-358.

Svensen, H., Planke, S., Corfu, F., 2010. Zircon dating ties NE Atlantic sill emplacement to initial Eocene global warming. Journal of the Geological Society 167, 433-436.

Thomson, K., Hutton, D., 2004. Geometry and growth of sill complexes: Insights using 3D seismic from the North Rockall Trough. Bulletin of Volcanology 66, 364-375.

Travis, C.J., Harrison, H., Hudec, M.R., Vendeville, B.C., Peel, F.J., Perkins, B.F., 1995. Origin of minibasins by multidirectional extension above a spreading lobe of allochthonous salt, Salt, sediment and hydrocarbons: SEPM Foundation, Gulf Coast Section. 16th Annual Research Conference Program with Papers, p. 135.

Valentine, G.A., Krogh, K.E., 2006. Emplacement of shallow dikes and sills beneath a small basaltic volcanic center–The role of pre-existing structure (Paiute Ridge, southern Nevada, USA). Earth and Planetary Science Letters 246, 217-230.

Vogt, P.R., 1997. Hummock fields in the Norway Basin and Eastern Iceland Plateau: Rayleigh-Taylor instabilities? Geology 25, 531-534.

Walker, R.J., 2016. Controls on transgressive sill growth. Geology 44, 99-102.

Walsh, J., Bailey, W., Childs, C., Nicol, A., Bonson, C., 2003. Formation of segmented normal faults: a 3-D perspective. Journal of Structural Geology 25, 1251-1262.

Walsh, J.J., Watterson, J., 1991. Geometric and kinematic coherence and scale effects in normal fault systems. Geological Society, London, Special Publications 56, 193-203.

Watterson, J., 1986. Fault dimensions, displacements and growth. Pure and Applied Geophysics 124, 365-373.

Zhang, Y., Xu, Z., Zhu, M., Wang, H., 2007. Silicate melt properties and volcanic eruptions. Reviews of Geophysics 45.

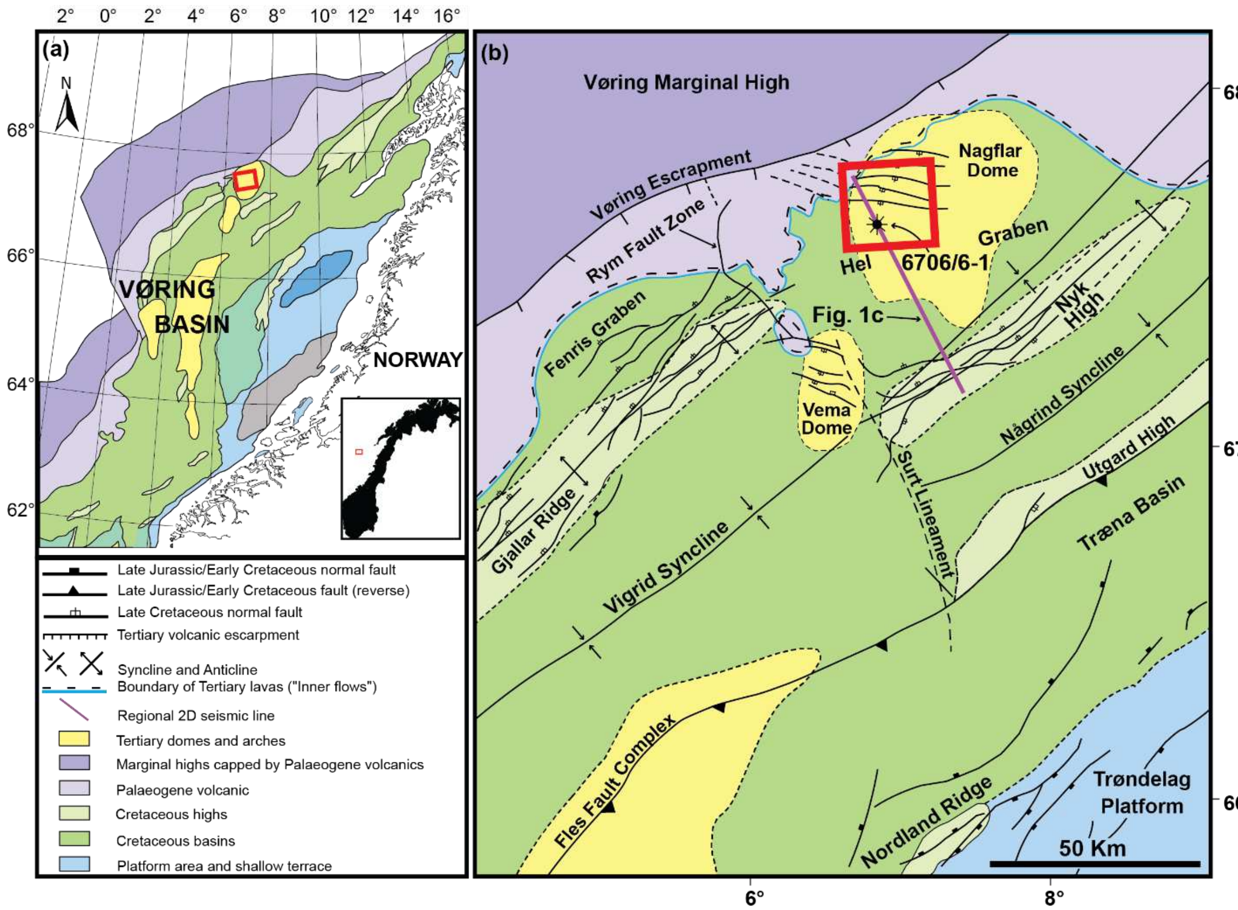

Figure 1: (a) Regional map showing the structural elements of the Vøring Basin. (b) The location of the study area is shown in the red rectangle. The inset shows the location of the study area in the context of the Norwegian coast. (c) NW-SE regional 2D seismic line across study area showing several structural elements such as forced fold, hydrothermal vent complex and inversion structures marked by reflections showing snake-head geometries (after Omosanya et al., 2017b). The yellow rectangle on the profile is the location of the 3D seismic cube used in this study.

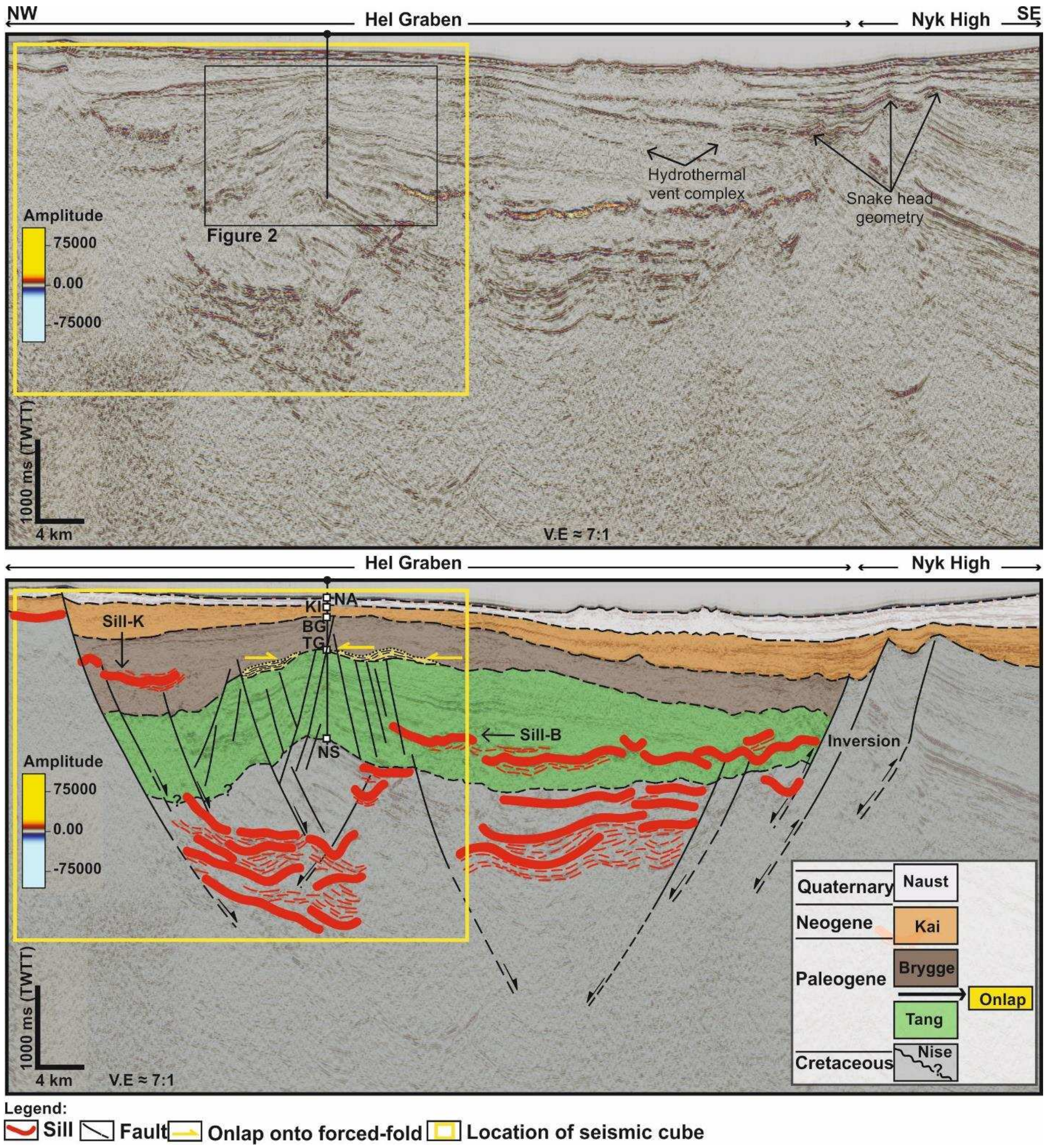

Figure 1: (Continue)

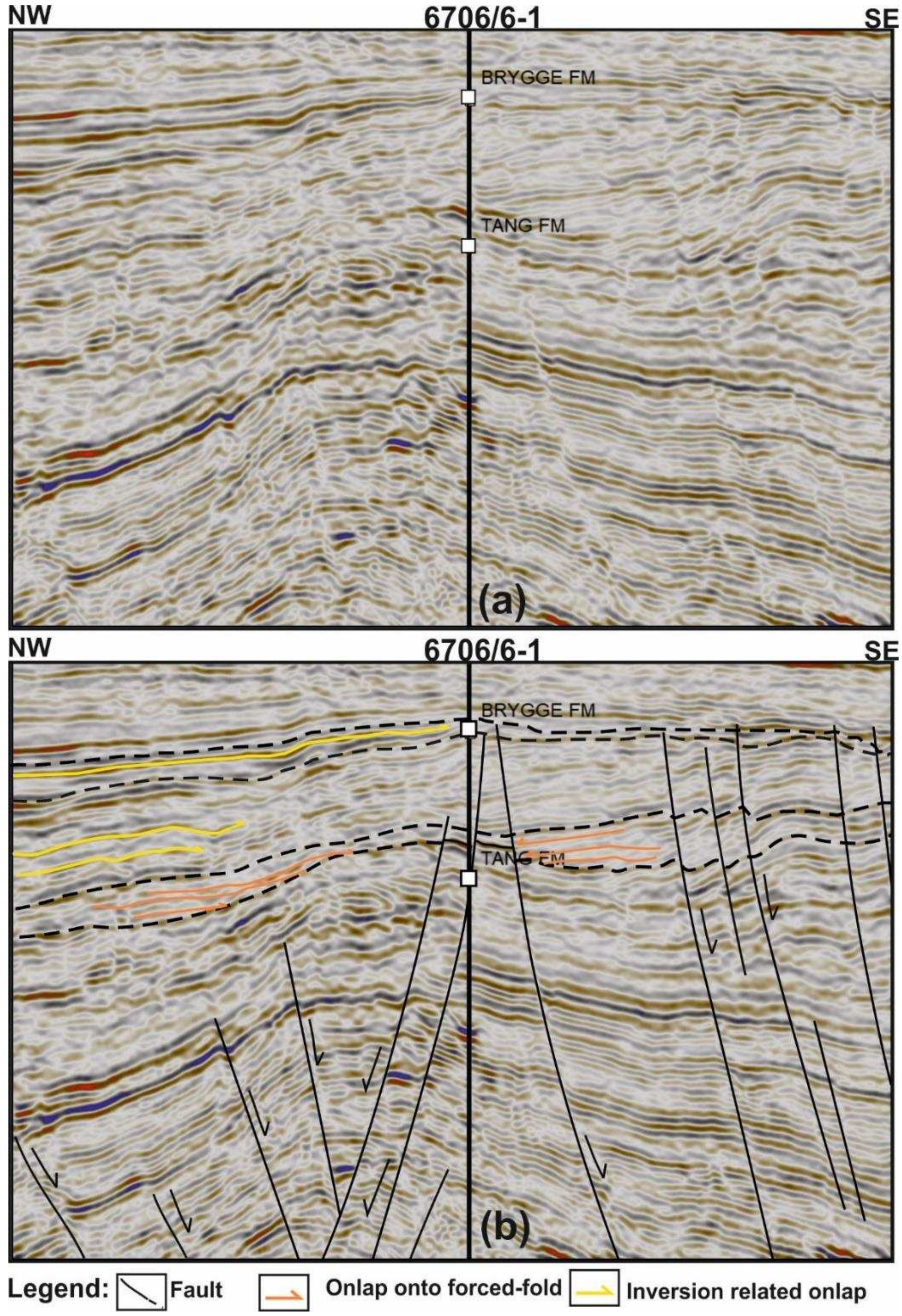

Figure 2: (a) Uninterpreted and (b) Interpreted seismic sections showing onlap reflections above the regional forced fold in the study area and younger faults that postdate emplacement of magmatic sills and evolution of the forced fold.

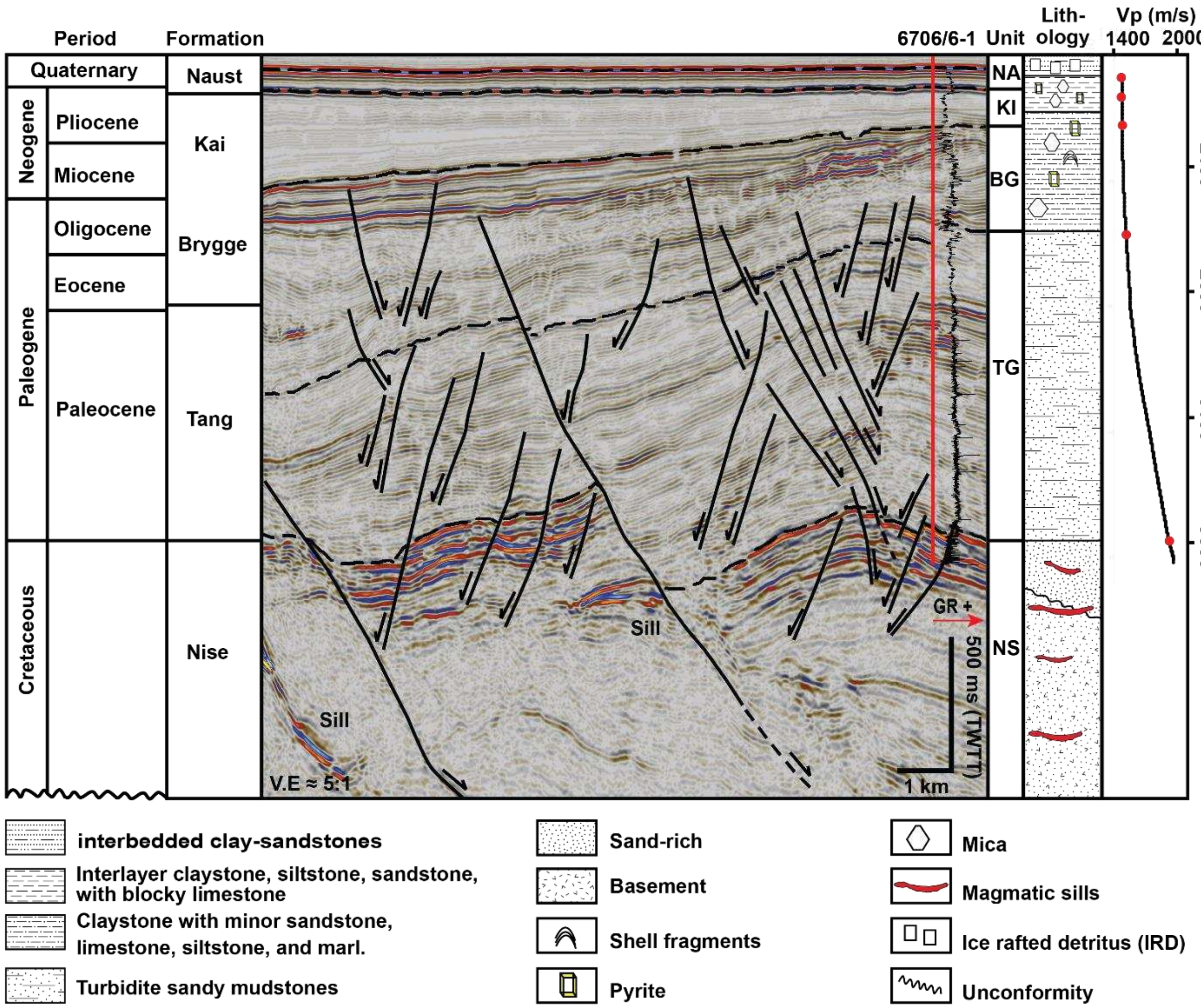

Figure 3: A seismic-lithostratigraphic chart showing the five principal units interpreted in the study area, ranging from upper Cretaceous to Quaternary in age. These include Naust Formation (NA); Kai Formation (KI), Brygge Formation (BG); Tang Formation (TG); Nise Formation (NS). Majority of the sills are well-distributed at an interval between BG and NS. Seismic-to-well tie was done using borehole 6706/6-1.

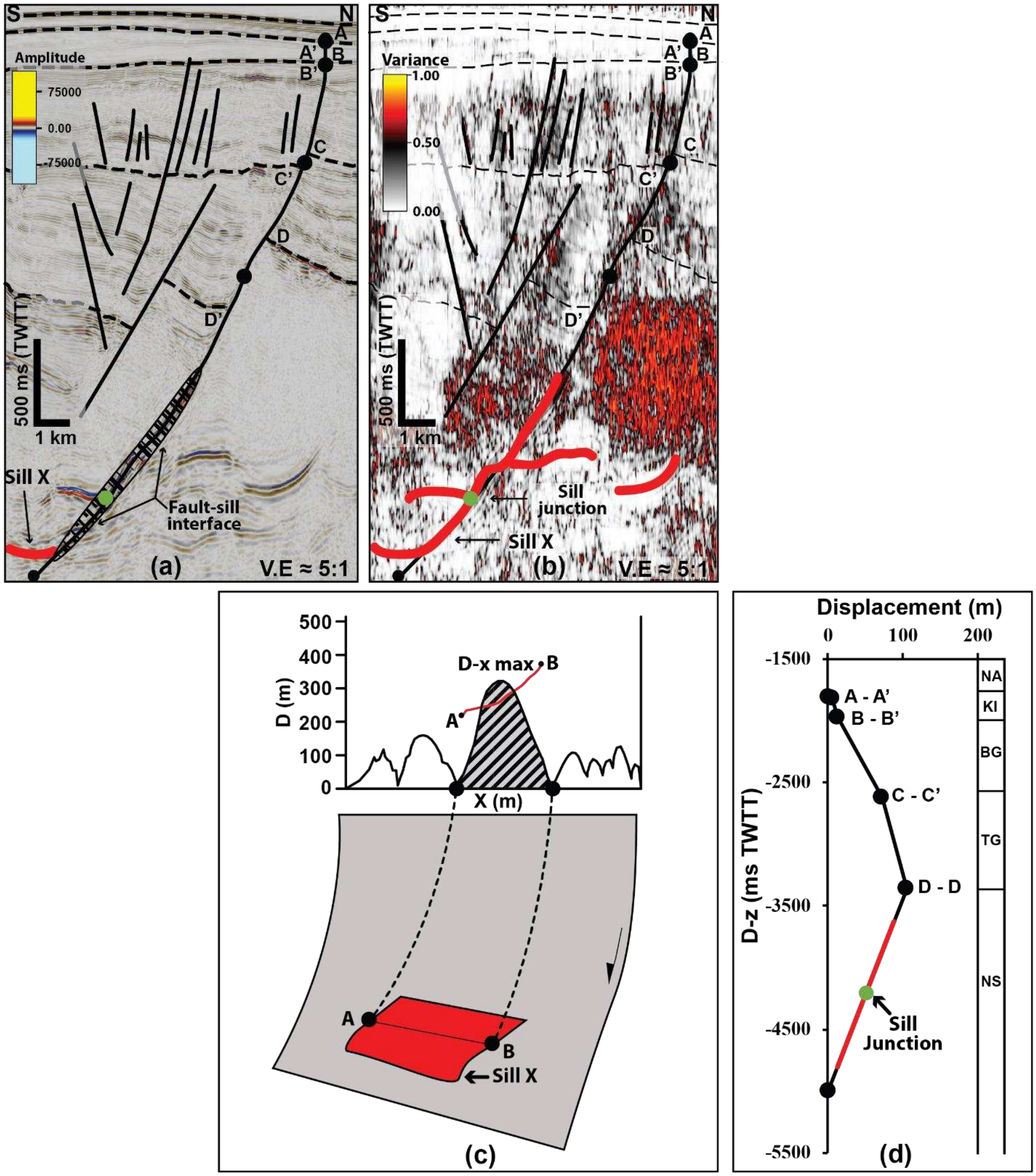

Figure 4: Methods for assessing the influence of sill emplacement on fault displacement in the study area (a) Original amplitude seismic section. (b) Variance attribute section to map both faults and sills. (c) Displacement-distance plot for assessing the influence of sill intrusion on fault kinematics and vice versa. The presence of sill-sill junction correlates to the area under displacement maximum. (d) D-z for understanding the influence of sill intrusion on fault propagation history. The points of sill intrusion along the fault surface are marked with a red line.

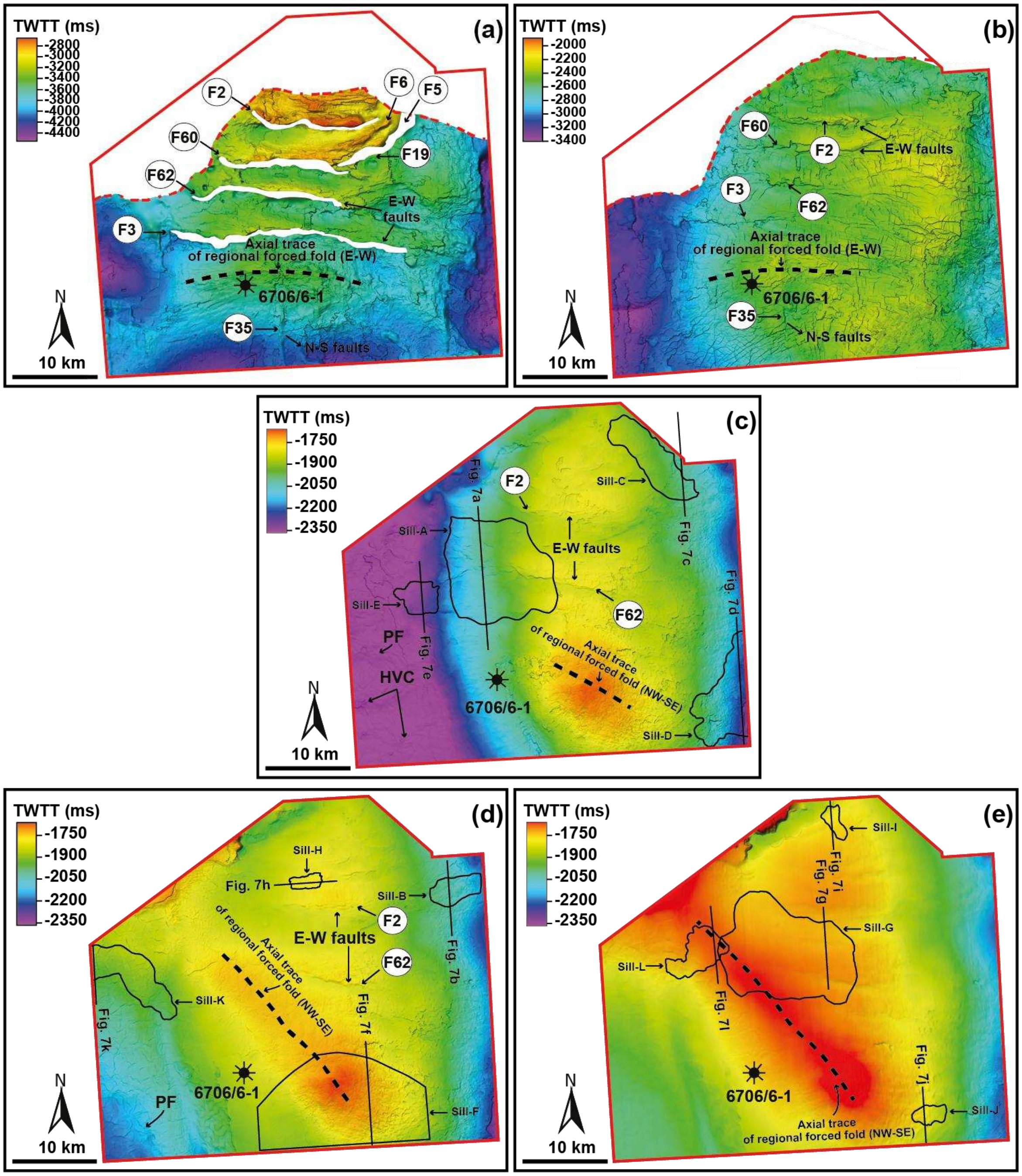

Figure 5: Time structure of five well tops. (a) The top of Nise Formation (NS) is affected by several Late Cretaceous to Early Eocene extensional faults. (b) Deformation is complex throughout Tang Formation (TG). (c) The top of Brygge Formation (BG) is predominated by polygonal faults and hydrothermal vents. (d) Polygonal faults are common in Kai Formation (KI). These faults are compaction and dewatering driven non-tectonic normal faults. (e) The top Naust Formation (NA) is typically unfaulted and only record Cenozoic compressional events. The axial trace of the forced fold is oriented in NW-SE contrary to the E-W orientation of the folds in the lower formations (i.e., Nise and Tang Formations). Also, it should be noted that the regional 2D seismic line (Figure 1c) runs through the axial trace of the fold of Figure 5c, 5d and 5e.

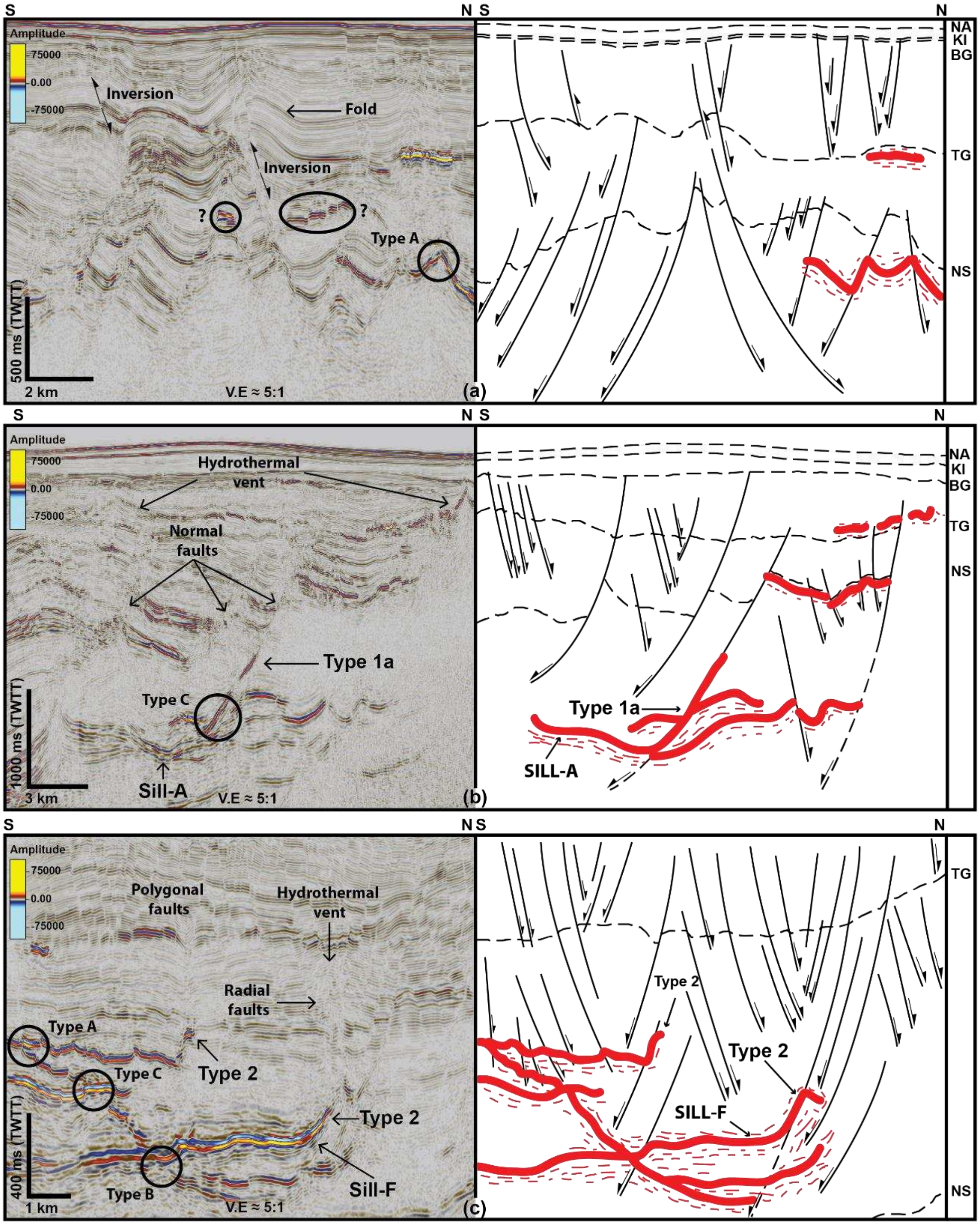

Figure 6: Seismic sections illustrating the interpreted seismic/stratigraphic units, faults and magmatic sills in the study area. Importantly, we show the end member fault-sill intersection geometries (a) Inversion fold structure caused by tectonic compression in the Late Eocene to Oligocene; (b) Saucer-shaped sill (Sill-A) ascending through a fault created a Type 1a fault-sill intersection geometry. (c) The seismic section shows sill network associated with Sill-F, polygonal and radial faults, steps and hydrothermal vents in the study area.

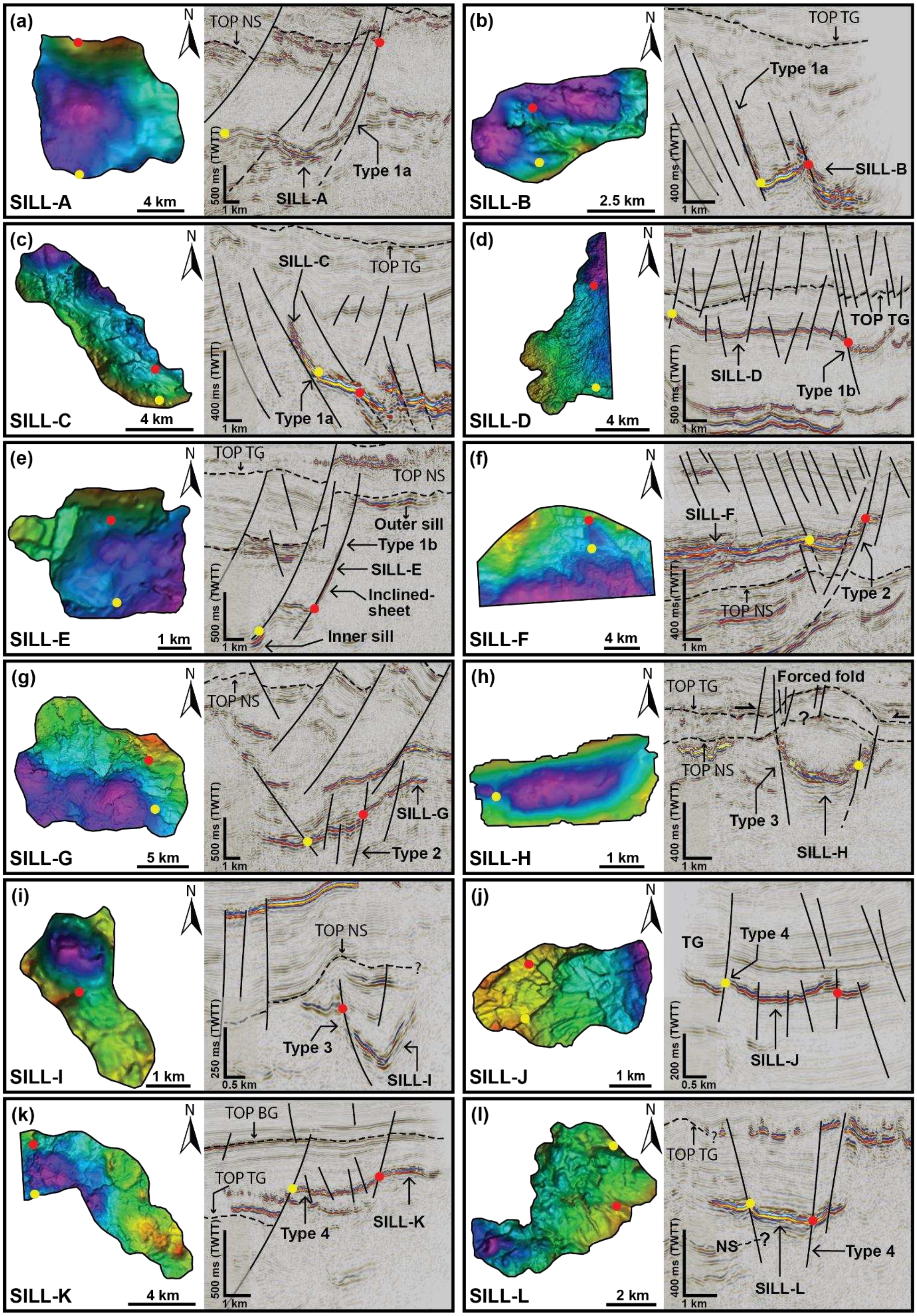

(a)
TOP NS
Type 1a
SILL-A
500 ms (TWTT)
1 km
SILL-A
4 km
(b)
TOP TG
Type 1a
SILL-B
400 ms (TWTT)
1 km
SILL-B
2.5 km
(c)
SILL-C
TOP TG
400 ms (TWTT)
1 km
Type 1a
SILL-C
4 km
(d)
TOP TG
SILL-D
Type 1b
500 ms (TWTT)
1 km
SILL-D
4 km
(e)
TOP TG
TOP NS
Outer sill
Type 1b
SILL-E
Inclined-sheet
Inner sill
500 ms (TWTT)
1 km
SILL-E
1 km
(f)
SILL-F
TOP NS
Type 2
400 ms (TWTT)
1 km
SILL-F
4 km
(g)
TOP NS
SILL-G
Type 2
500 ms (TWTT)
1 km
SILL-G
5 km
(h)
TOP TG
Forced fold
TOP NS
Type 3
SILL-H
400 ms (TWTT)
1 km
SILL-H
1 km
(i)
TOP NS
Type 3
SILL-I
250 ms (TWTT)
0.5 km
SILL-I
1 km
(j)
TG
Type 4
SILL-J
200 ms (TWTT)
0.5 km
SILL-J
1 km
(k)
TOP BG
TOP TG
Type 4
SILL-K
500 ms (TWTT)
1 km
SILL-K
4 km
(l)
TOP TG
NS
SILL-L
Type 4
400 ms (TWTT)
1 km
SILL-L
2 km

Figure 7: Seismic sections showing the twelve interpreted sills in the study area. Geometrically, the sills include saucer-shaped; (a-e); transgressive (f and g); radially symmetrical saucer-shaped (h and i) and strata concordant (j-l). As regards to fault-sill intersection geometries (Table 2), these include Type 1a (a-c), Type 1b (d-e), Type 2 (f-g), Type 3 (h and i) and Type 4 (j, k and l). Note: The locations of the seismic lines are shown in Figure 5.

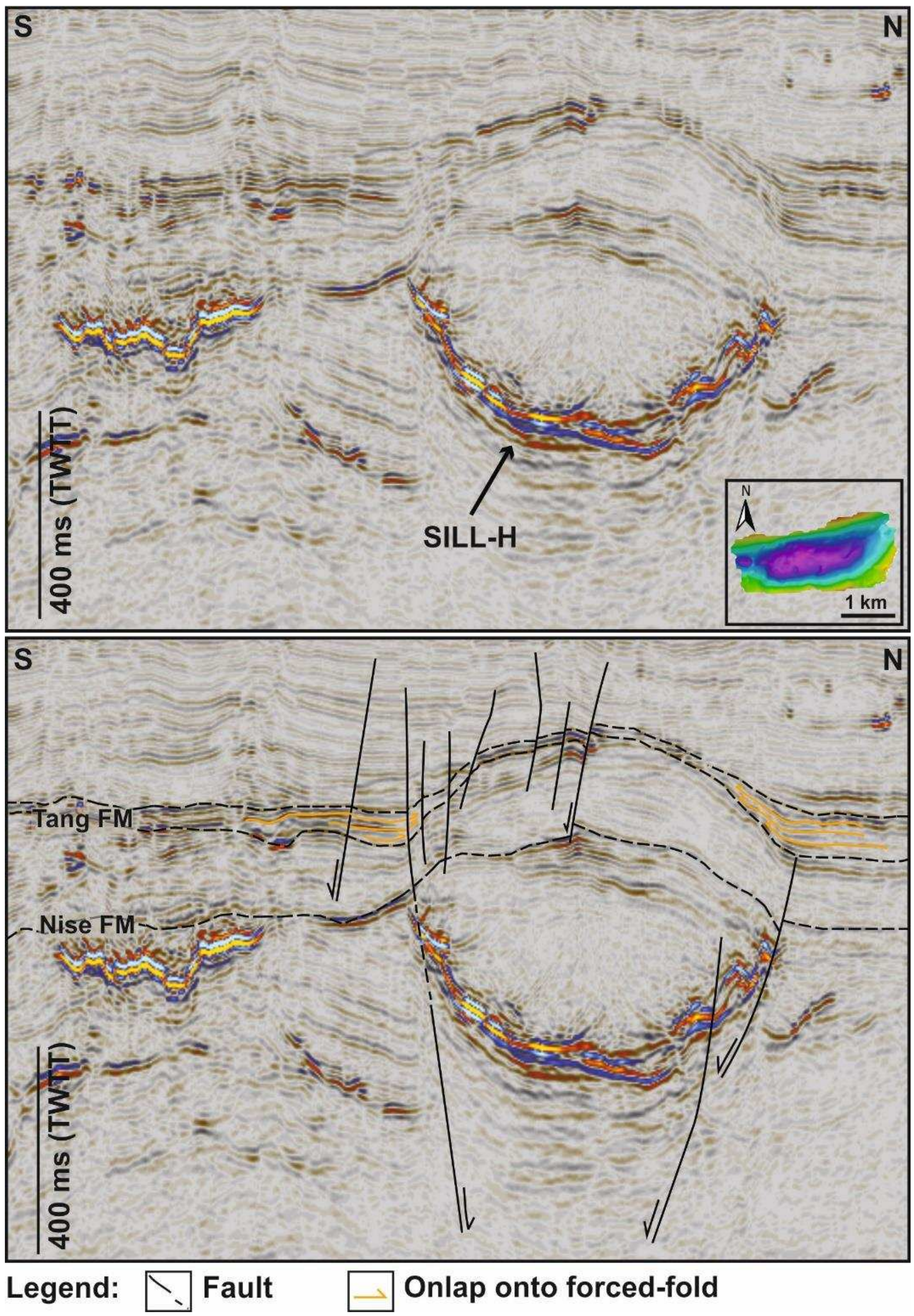

Figure 8: Uninterpreted and interpreted seismic section showing a saucer-shaped intrusion that is overlain by at a forced fold at the Top Tang Formation, which is in turn onlapped by strata of the Brygge Formation.

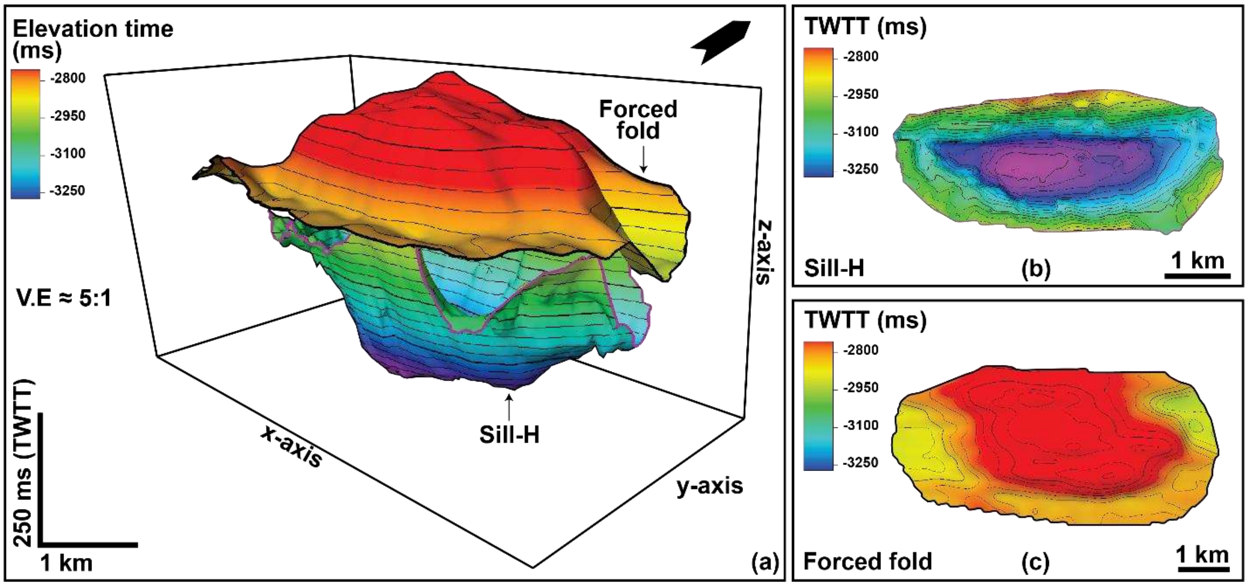

Figure 9: (a) 3-D image showing how the lateral limits of this forced fold coincide with the spatial extent of the underlying sill lateral. Forced folds in the study area are direct manifestation of magmatic emplacement (b) and (c) are the structural map of Sill-H and the overlying forced fold, respectively.

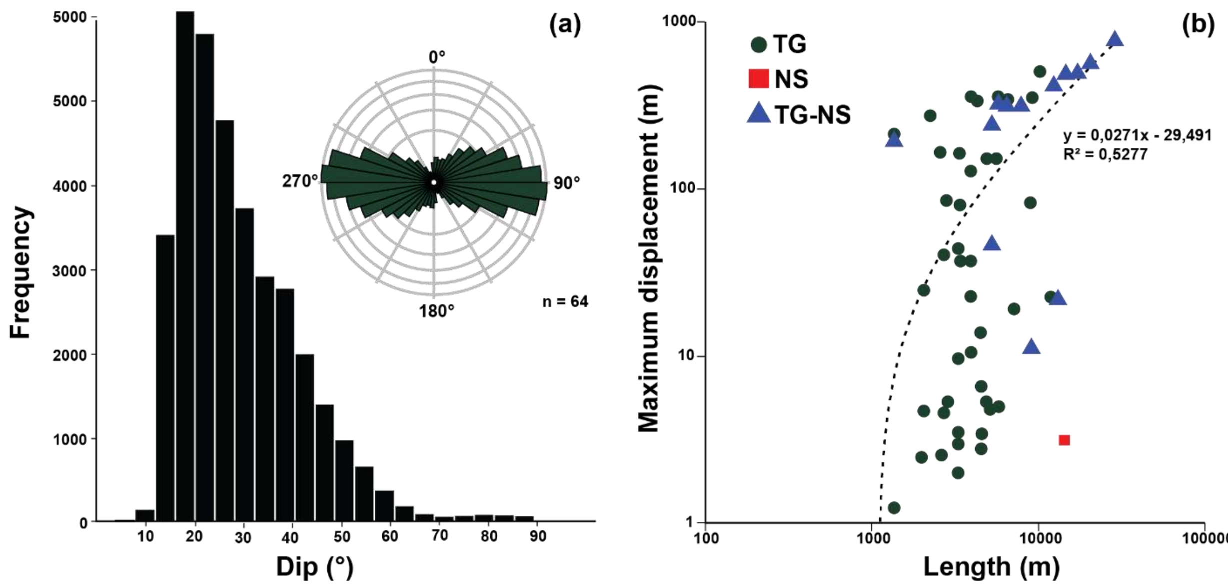

Figure 10: (a) Bar chart showing the distribution of faults' dip and azimuth in the study area. (b) Plots of maximum displacement against fault length for the tectonic faults discussed in the text. Displacement measurements were taken along the TG (Tang formation), NS (Nise Formation) and TG-NS (Nise-Tang Formations). Note: Fault attitude (strike and dip) are estimated as dislocation element, which will have opposing displacement vector (both side of triangles) on the selected surface and observation points of a surrounding faults, allowing displacement, dip and azimuth distribution of faults in the study area to be measured.

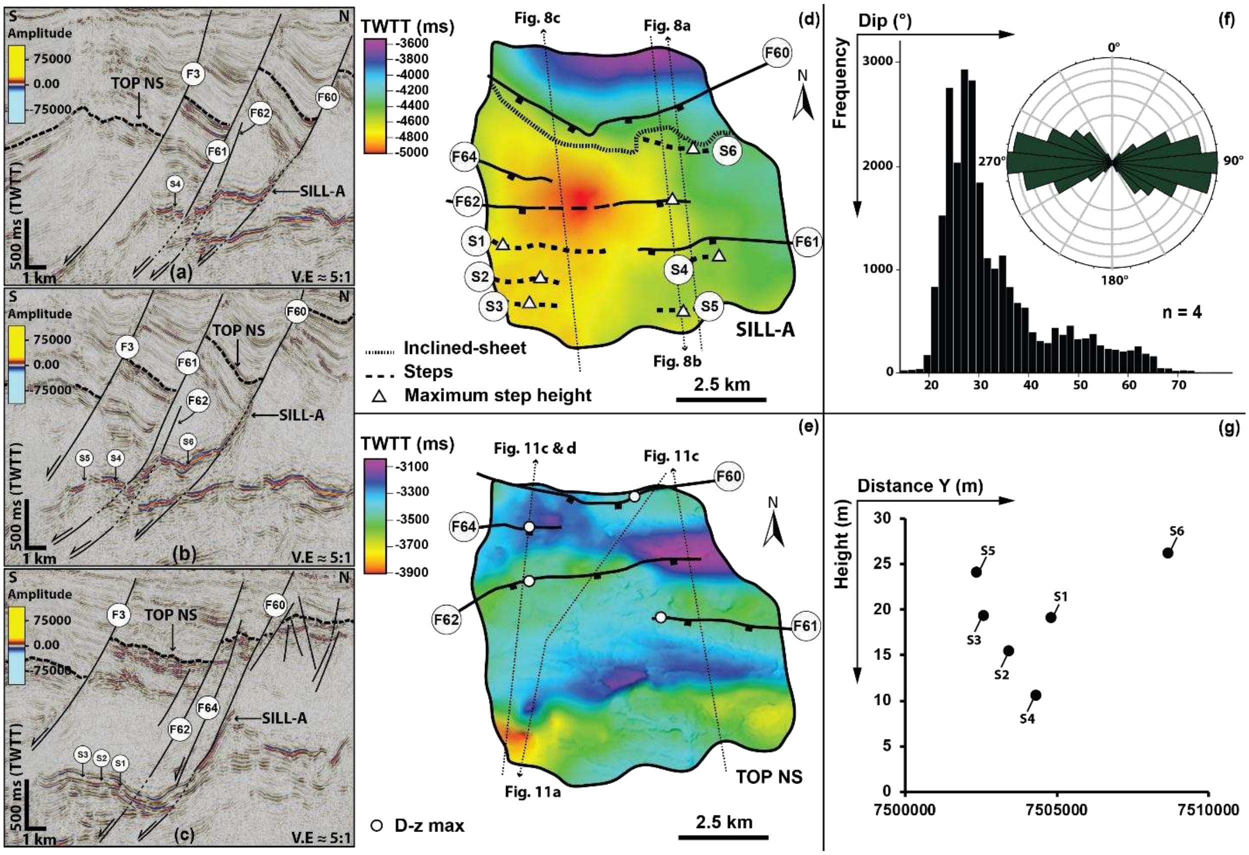

Figure 11: (a-c) Interpreted seismic sections showing fault-sill relationships and steps for Sill-A; (d) Time structure map of Sill-A displaying its associated faults and steps; (e) Time structure map of the Nise Formation (NS) restricted to the extent of Sill-A and areas of the D-z plot. (f) Each triangle on NS-time structure map represents a single dislocation element which is used to calculate the fault dip and azimuth distribution; (g) The maximum height of the measured steps, which typically increases to the northern part of the study area.

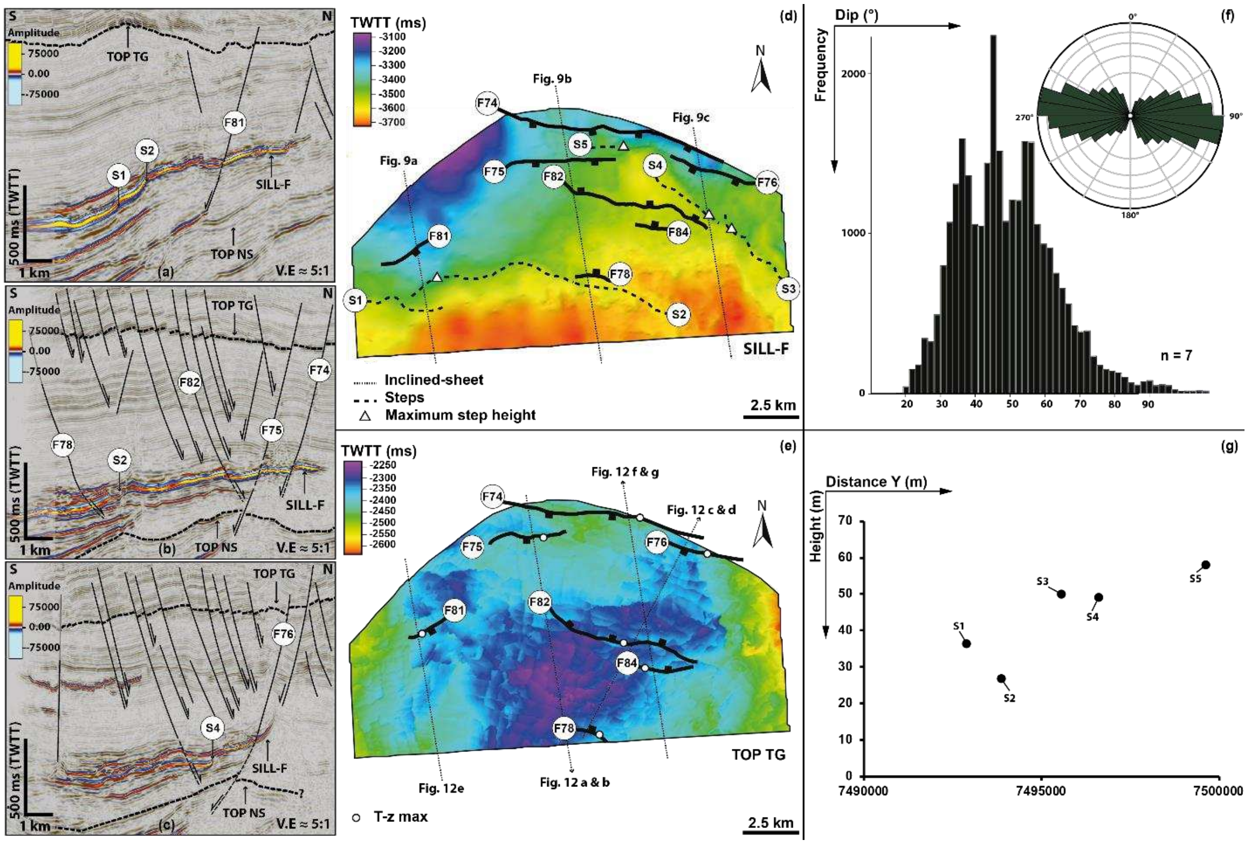

Figure 12: (a-c) Interpreted seismic sections showing fault-sill relationships and steps for Sill-F; (d) Time structure map of Sill-F; (e) Time structure map of the Tang Formation (TG) bounded by the boundary of Sill-F with D-z max plot; (f) Fault dip and azimuth distribution; (g) The maximum height of the measured steps, which typically increases to the northeastward.

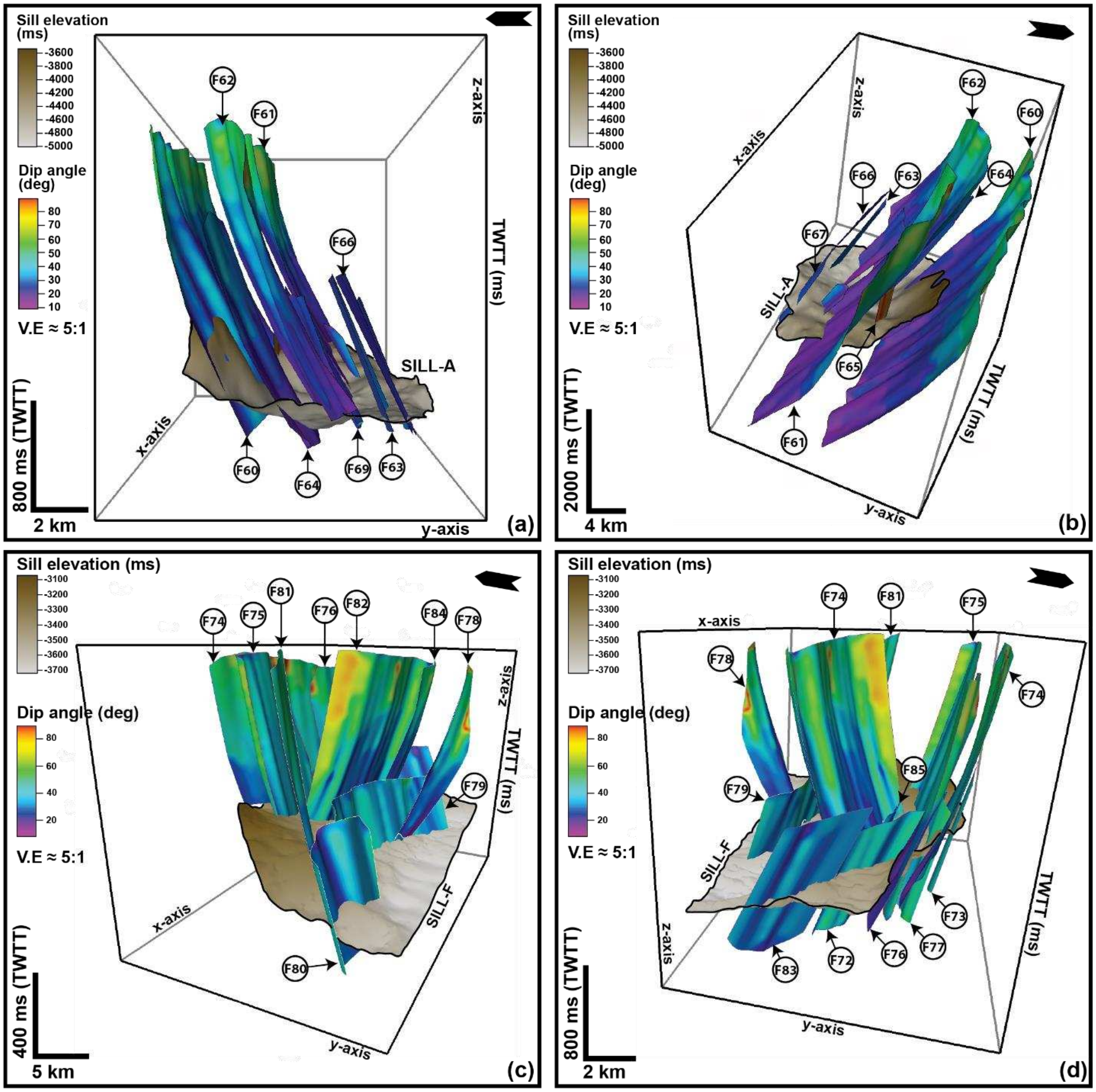

Figure 13: 3-D diagrams showing the cross-cutting relationship between (a and b) Sill-A and the four selected tectonic faults and (c and d) Sill-F and the seven tectonic faults used for the D-x plots.

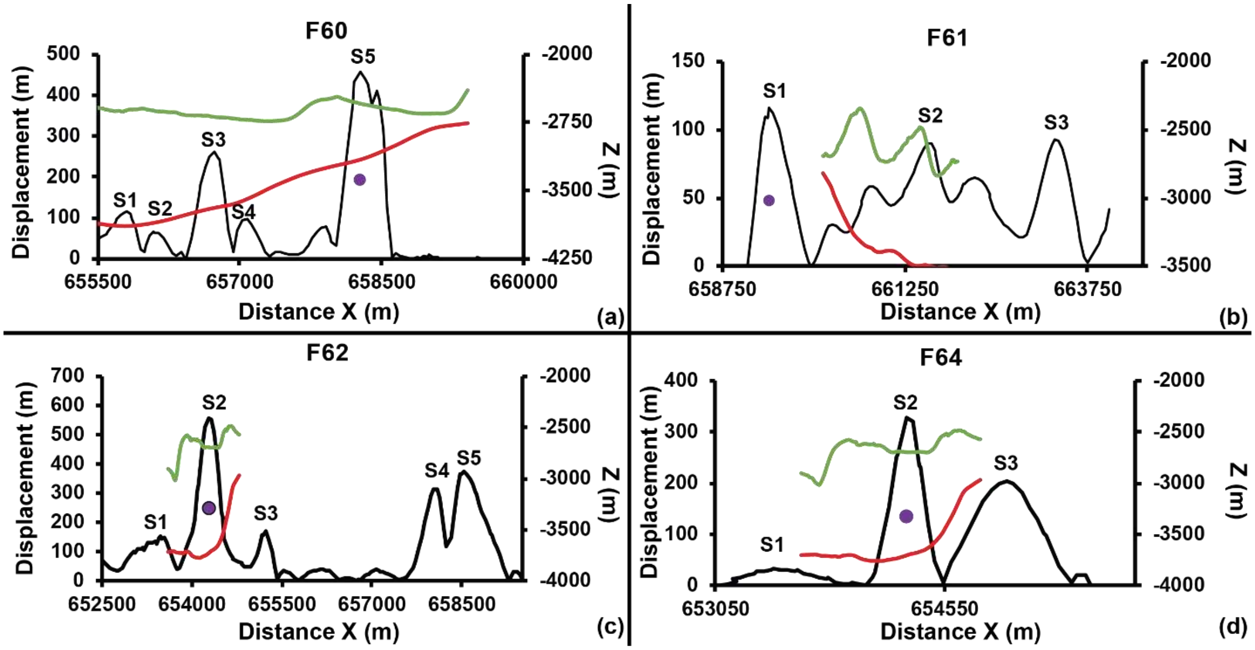

Figure 14: D-x profiles plotted along the Nise Formation (NS). The purple dot is the position of the D-z profiles, which also coincides with the point of D-max on the D-x plot. The red and green lines represent the depths of occurrence for Sill-A and NS directly above the intrusion, respectively. The Sn+1 represents marked fault segments.

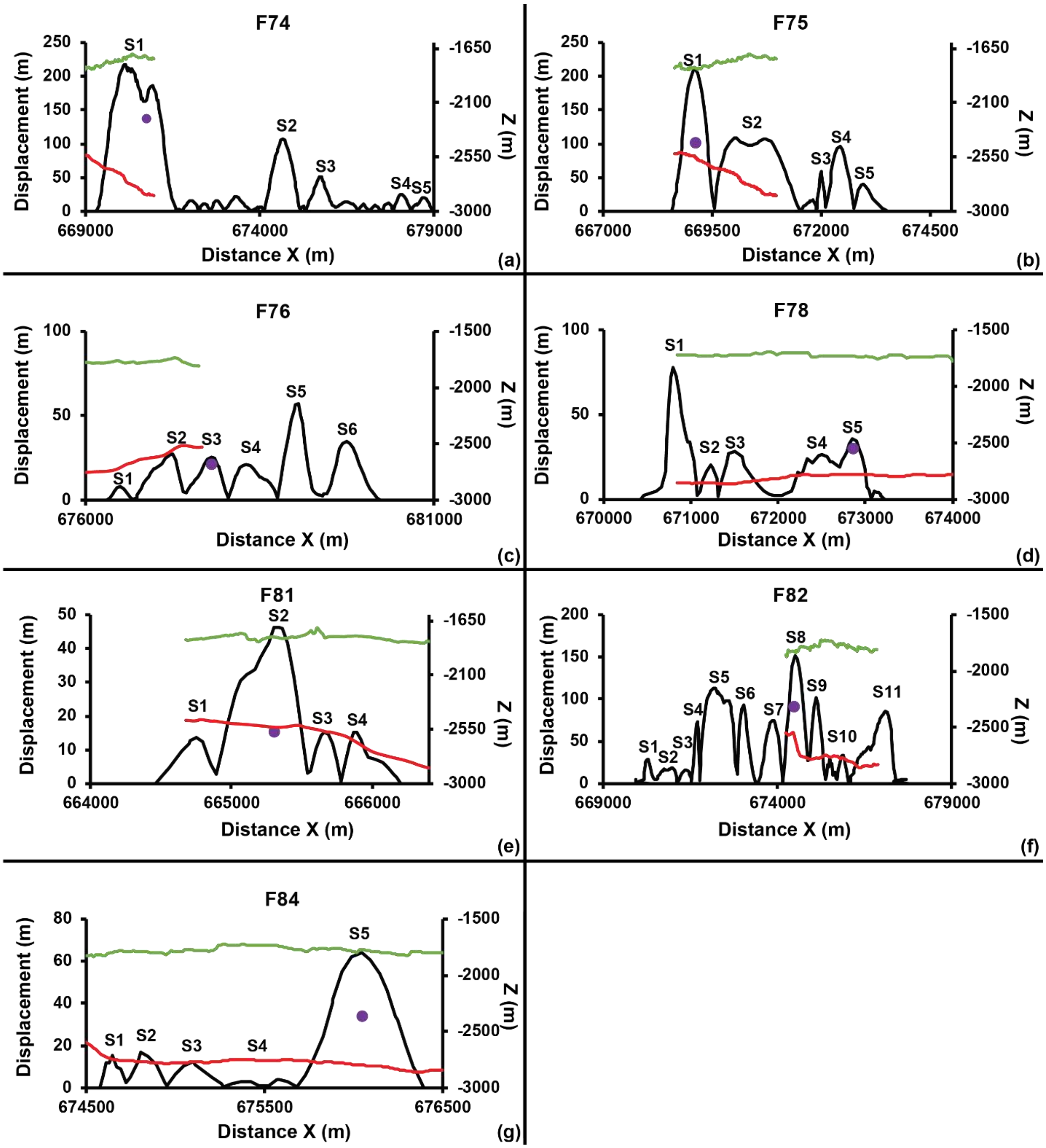

Figure 15: D-x profiles (black line) derived based on Tang Formation (TG). The purple dot is the maximum D-z profiles, taken after D-x maximum. The red and green lines represent depths of occurrence for Sill-F and TG, respectively. The Sn+1 represents marked fault segments.

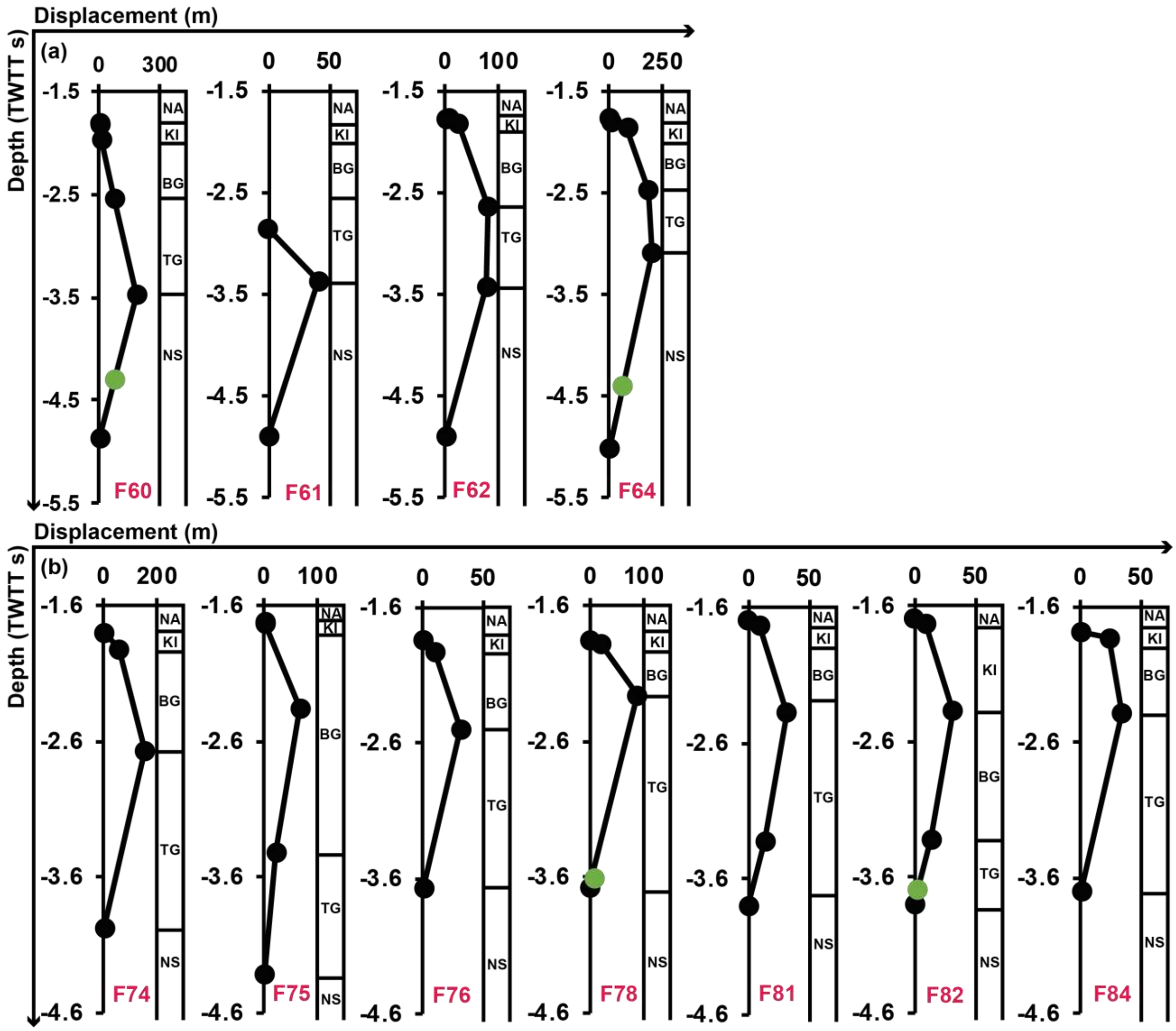

Figure 16: Displacement-depth (D-z) plots for the faults associated with (a) Sill-A and (b) Sill-F. The green dots are where the sill-sill junction occurred.

Table 1: Morphometry data for magmatic sills interpreted in the study area.

Sill name	Area (km^2)	Length (km)	Long Axis (L) (km)	Short Axis (S) (km)	Aspect ratio (L/S)	Maximum Depth (ms TWTT)	Geometry
Sill-A	113	55	11.07	11.72	0.94	5015	SS
Sill-B	19	19	7.05	2.82	2.50	3615	SS
Sill-C	39	33	12.93	3.27	3.95	3743	SS
Sill-D	49	40	14.04	4.11	3.41	3346	SS
Sill-E	16	19	5.62	4.40	1.27	4514	SS
Sill-F	180	66	18.80	10.53	1.79	3772	TS
Sill-G	156	58	17.66	11.58	1.52	5790	TS
Sill-H	6	12	4.16	1.40	2.97	3236	RS
Sill-I	6	12	4.37	1.31	3.33	2892	RS
Sill-J	31	25	8.61	4.78	1.80	3364	SC
Sill-K	42	35	12.96	4.12	3.14	2974	SC
Sill-L	24	26	7.31	1.75	4.17	3324	SC

Note: Maximum depth represents the uppermost limit of the sills. Note: SS: saucer-shaped; RS: radially symmetrical saucer-shaped; TS: transgressive; SC: strata-concordant.

Table 2: Simple model of fault-sill intersection geometries in the study area.

Interaction type	Type 1a	Type 1b	Type 2	Type 3	Type 4
Geometry	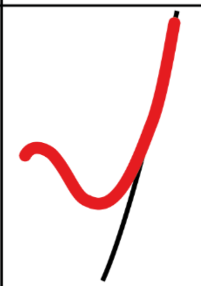	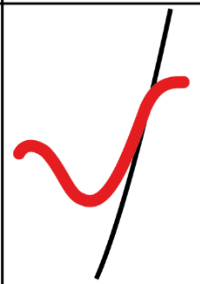	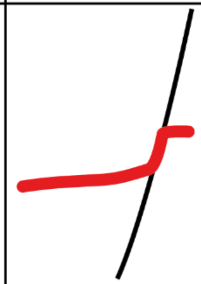	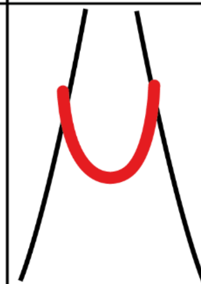	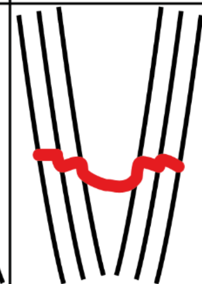
Sill Type	Lobate/ Saucer- shaped	Lobate/ Saucer- shaped	Strata-concordant, transgressive	Lobate/ Saucer- shaped	Lobate/ Saucer- shaped
Associated fault	Normal fault	Normal fault	Normal fault	Normal fault	Polygonal fault
Fault dip (°)	20° - 45°	20° - 45°	20° - 45°	20° - 45°	20° - 65°
Fault Strike	160° - 200°	160° - 200°	160° - 200°	160° - 200°	130° - 200°

Fault dip of 20^0 to 45^0 suggest the fault are low-angle normal faults while higher fault dip of up to 65^0 are typical of high angle normal faults.